ACS Sustainable Chemistry & Engineering

pubs.acs.org/journal/ascecg

Research Article

Highly Stable Single-Phase FeCoNiMnX (X = Cr, Mo, W) High-Entropy Alloy Catalysts with Submicrometer Size for Efficient Oxygen Evolution

Peng Li, Bozhao Wu, Kaifa Du, Ze Liu, Enlai Gao, Huayi Yin,* and Dihua Wang*

Cite This: https://doi.org/10.1021/acssuschemeng.3c04499

Read Online

ACCESS | Metrics & More | Article Recommendations | Supporting Information

ABSTRACT: The activity and stability of oxygen evolution reaction (OER) catalysts are often trade-offs and are both size-dependent. Theoretical calculations have predicted that some noble-metal-free high-entropy alloys (HEAs) are promising OER catalysts. However, their catalytic properties have not been proven because of the lack of a facile method to synthesize small-sized homogeneous HEA particles. Here, submicrometer-sized single-phase FeCoNiMnW HEA particles were prepared by electrochemical metallization in 900 s (at 900 °C). FeCoNiMnW shows the best OER activity (η = 355 mV at 500 mA cm^{-2}) and durability of the three HEAs because the large total density of states of FeCoNiMnW accelerates the electrons' transport speed for OER. More importantly, the single-phase FeCoNiMnW continuously operated for 50 days at 500 mA cm^{-2} with an almost unchanged overpotential. Overall, this work offers a rapid and simple method to prepare various effective and long-lasting single-phase HEA catalysts with controllable sizes and enhanced OER performances.

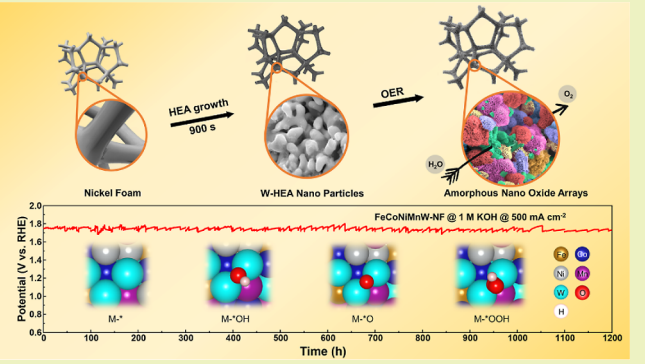

KEYWORDS: *HEA, particle size, FeCoNiMnW, high current density, OER*

INTRODUCTION

Water electrolyzers are a promising solution to achieve the green production of hydrogen.[1] To minimize the energy consumption of the electrolyzer, both the hydrogen evolution reaction (HER) at the cathode and the oxygen evolution reaction (OER) at the anode need affordable and efficient catalysts, especially for the OER which has more complex electrochemical steps.[2,3] Currently, noble metals like Ir and Ru are always used as stable catalysts to reduce the overpotential of electrochemical catalysis.[4,5] Besides the noble metals, transition-metal (TM) oxides,[6,7] hydroxides,[8] nitrides,[9] and phosphates[10] are promising OER candidate catalysts to reduce the cost. Among various TM-based catalysts, high-entropy alloys (HEAs) are emerging materials and gaining immense attention due to their great mechanical and catalytic qualities.[11] Nevertheless, some promising HEA catalysts can only be predicted due to the lack of facile synthesis methods to synthesize single-phase HEAs.[12,13] Therefore, the development of a facile method to mediate the composition, particle size, and structures to control the catalytic performance of HEAs is crucial.

Among the different states of HEAs, HEA nanoparticles (HEA NPs) can fully exert the synergistic effect and provide more active sites and tunable binding energies for OER.[14,15] Until now, HEAs are usually prepared by the methods of arc melting,[16] mechanical ball milling,[17] solvothermal[18] and fast bed pyrolysis, etc.[19] However, there are three challenges to preparing HEA NPs for the use of OER catalysts using these methods. First, the preparation of uniform HEAs consisting of elements with great disparity in physicochemical properties (i.e., density (ρ), melting point (mp), atomic radius (r), electronegativity (χ), and mixing enthalpy (ΔH), etc.),[20,21] which will result in significant phase separation and segregation in the alloy.[22,23] Second, reducing the particle size of HEAs is difficult because the long preparation time and high temperature (higher than mp) result in the growth of the particles.[24] Moreover, an extreme cooling rate is required, and the multistep preparation process increases the synthesis complexity and costs.[25] Third, the durability of the particulate catalyst is limited by the weak connection between the active particles and substrates, particularly when there are significant current densities present where ferocious bubbles make the alloy particles easily slip off the substrates. It remains a challenge to

Received: July 22, 2023
Revised: August 31, 2023

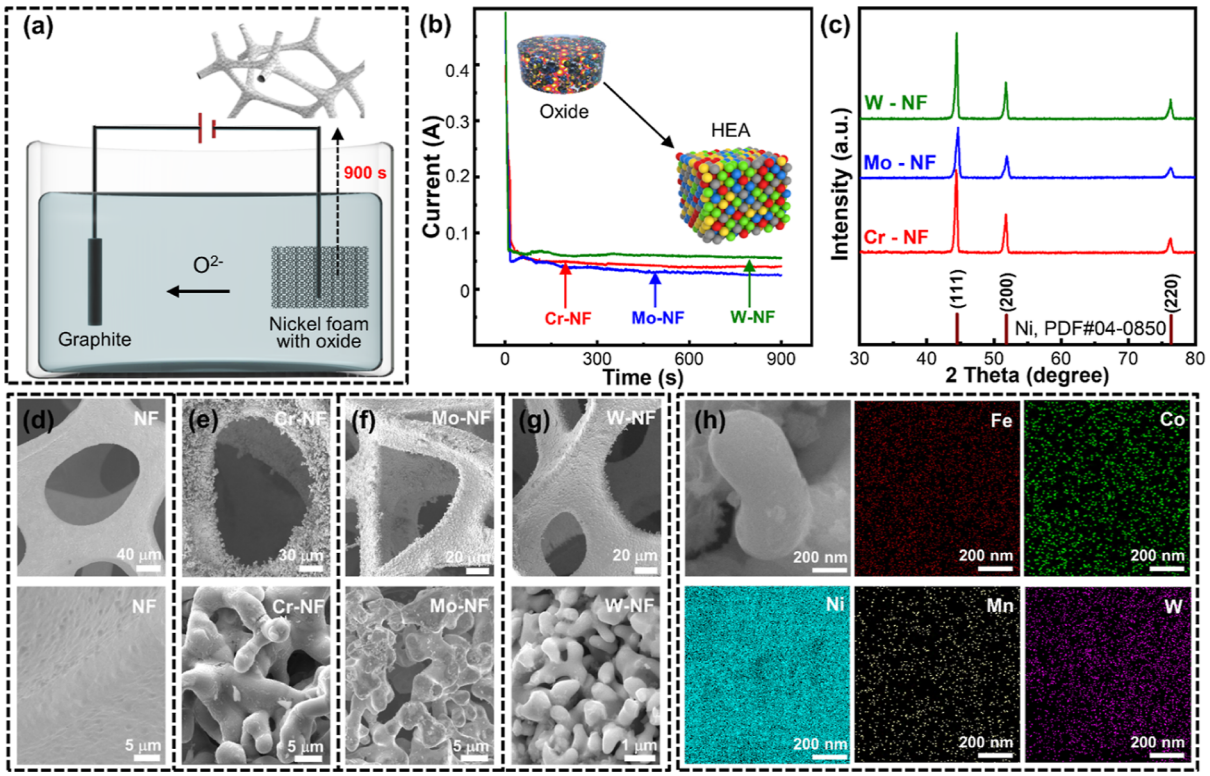

Figure 1. HEAs preparation and characterization. (a) Schematic illustration of the creation of high-entropy alloys attached to nickel foam in molten $CaCl_2$. (b) Electrolysis (c) XRD patterns, and SEM images of (d) NF, (e) Cr-NF, (f) Mo-NF, and (g) W-NF. (h) EDS mapping of W-NF.

synthesize single-phase HEAs with decreased particle size with both high efficiency and durability.

In this paper, we rapidly prepared a series of FeCoNiMnX (X = Cr, Mo, W) HEAs by molten salt electrolysis of oxide mixtures coated on nickel foam (NF). The diameters of HEAs can be tailored by modifying the composition of the oxide precursor. In addition, the in situ metallization process rendered a robust connection between FeCoNiMnX HEAs and the nickel foam. The OER performances in terms of activity and durability were performed. First-principles calculations were done to determine the internal mechanism of the OER. Finally, a big electrode (40 × 500 mm) was prepared in the same manner to verify the possibility of scaling up the electrochemical method.

EXPERIMENTAL SECTION

The self-supporting FeCoNiMnCr, FeCoNiMnMo, and FeCoNiMnW HEAs were electrolytic metal oxides (Fe_2O_3, Co_3O_4, NiO, MnO_2, Cr_2O_3, MoO_2, WO_2) on nickel foam cathodes in molten $CaCl_2$ at 900 °C. First, 5 g of equiatomic ratio oxides (Fe_2O_3, Co_3O_4, NiO, MnO_2, Y (Y= Cr_2O_3 or MoO_2 or WO_2) were mixed with a planetary ball mill for 12 h. Second, 1 g of oxide mixture was placed in ultrasonically shaken alcohol (50 mL) to make the distributions. Third, clean nickel foam (10 mm × 10 mm × 1 mm) was put into the distributions for 5 min (Figure S1a) or until the alcohol dried (Figure S1b); during this process, the samples were continuously dispersed by ultrasonically shaking. Another way to handle the samples is by putting the oxide mixture (1 g) on the nickel foam and wrapping it into a sandwich shape with fresh nickel foam (Figure S1c). Fourth, the electrolysis reductions were carried out in 500 g of $CaCl_2$ (ramping rate 5 °C min^{-1}) at 900 °C with graphite (diameter: 20 mm, length: 100 mm) as an anode and nickel foam with oxide mixtures as the cathode under constant potential (2.0 V) and time (900 s). The nickel foam cathode was removed from $CaCl_2$ after each electron reduction and cooled to room temperature. Finally, the samples were then rinsed with deionized water after being prepared. The electrolysis was controlled by a battery test system (Shenzhen Newray Electronics Co. Ltd. China, CT-4008-5 V 6 A-S1). The HEA-NF in the scale-up experiment was 40 × 500 mm in scale with the method shown in Figure S1.

OER performances were carried out by CHI 1140C (Shanghai Chenhua Instrument Co. Ltd., China) with a trielectrode system (a double salt bridge Hg/HgO electrode as the reference electrode, the nickel foam with oxide mixture as the working electrode, and a graphite rod as the counter electrode) in 1.0 M KOH (O_2-saturated). The performance of the OER was investigated by linear sweep voltammetry (LSV, 2 $mV{\cdot}s^{-1}$), cyclic voltammetry (CV), and chronopotentiometry (CP). Electrochemical impedance spectroscopy (EIS) was measured by an electrochemical instrument (AUTO LAB, PGSTAT302N). The potentials in this paper refer to reversible hydrogen potential (RHE) according to the equation $E(\mathrm{RHE}) = E(\mathrm{Hg/HgO}) + \mathrm{pH} \times 0.0591 + 0.098$ with 85% iR compensation.

X-ray diffraction spectroscopy tested the crystal structures of the products (XRD, Rigaku MiniFlex 600). The morphologies and microstructures of the products were studied by transmission electron microscopy (TEM, Talos F200x) and scanning electron microscopy (SEM, Zeiss EVO LS-15) with energy-dispersive spectroscopy (EDS, Horiba 7021-H). The surface of the HEA was examined by X-ray photoelectron spectroscopy (XPS, Thermo ESCALAB 250XI).

The theoretical thermodynamic values in this work were obtained by the HSC 6.0 software. Vienna ab initio simulation software package (VASP) was used to calculated the spin-polarized first-principle.[26] A 500 eV energy cutoff was set for the plane-wave basis and projector augmented wave potentials.[27] The exchange–correlation functional was carried out by the Perdew–Burke–Ernzerhof[28] of the generalized gradient approximation.[29] A k-point sampling with a density >30 Å adopted the Monkhorst–Pack scheme[30] for the structural relaxations. A vacuum layer with a thickness of 20 Å was used to eliminate the electrostatic interactions. Both the locations of all ions and the unit cell characteristics of the pure HEA slab were loosened to reduce the atomic forces and total energy. To achieve a constant vacuum spacing while the cell can be

https://doi.org/10.1021/acssuschemeng.3c04499
ACS Sustainable Chem. Eng. XXXX, XXX, XXX−XXX

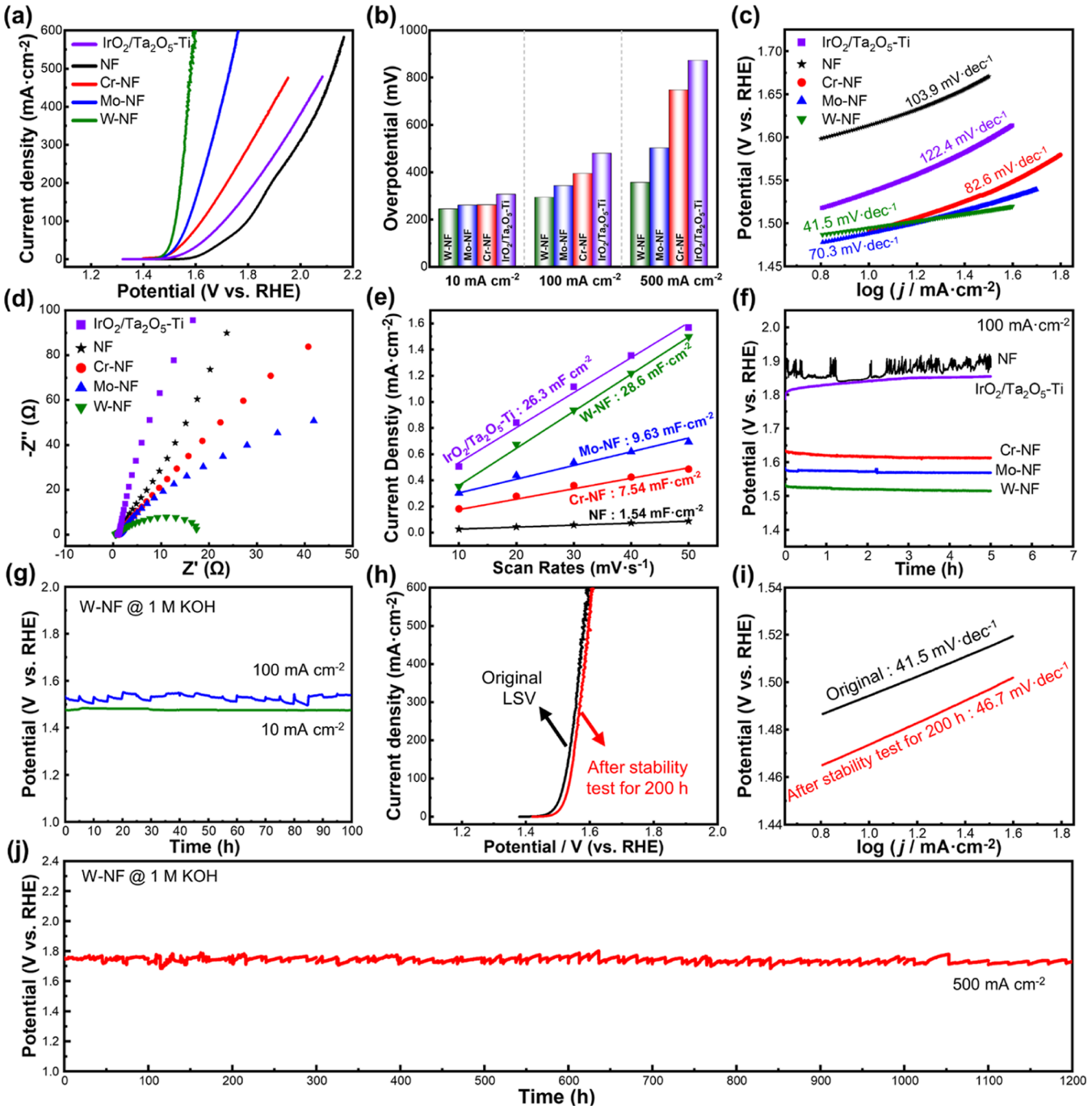

Figure 2. OER performances of the NF-based HEA electrodes in 1.0 M KOH. (a) Polarization curves, (b) overpotentials at 10, 100, and 500 mA cm^{-2}, (c) Tafel plots, (d) electrochemical impedance spectra, (e) double layer capacitances, and (f) durability tests at 100 mA cm^{-2} of NF, Cr-NF, Mo-NF, W-NF, and IrO_2/Ta_2O_5−Ti electrodes. (g) Stability test at 10 and 100 mA cm^{-2}, (h) polarization curves, and (i) Tafel plots before and after the stability test for 200 h of W-NF. (j) Stability test for continuous 1200 h of the W-NF electrode at 500 mA cm^{-2}.

optimized in the basal plane, the VASP code was modified. The positions of the top two layers of atoms and adsorbates were relaxed for the slab with the adsorbates. Besides, the force on each atom converged below 0.01 eV/Å, and the *k*-point sampling (density >40 Å) was used to calculate electronic structures.

RESULTS AND DISCUSSION

Preparation of Nickel Foam-Based HEA Electrodes. Self-supporting nickel foam-based FeCoNiMnCr (named Cr-NF), FeCoNiMnMo (named Mo-NF), and FeCoNiMnW (named W-NF) HEAs were prepared in a one-step molten salt electron of oxide reduction at 2.0 V for 900 s (Figure 1a). We prepared NF with oxides in three ways (Figure S1). The most suitable method is the dipping method (Figure S1a). Drying the alcohol caused oxides to deposit on the bottom (Figure S1b). The sandwich-shaped products were very nonuniform, and the alloy powder was extremely prone to detachment (Figures S1c and S2). Additionally, the dipping method can ensure an oxide loading of 0.02 g on the nickel foam (Table S1, three samples for each method, precisely calculating the sample mass before and after loading). In addition, the reduction current dropped to the background current after ∼200 s

https://doi.org/10.1021/acssuschemeng.3c04499
ACS Sustainable Chem. Eng. XXXX, XXX, XXX−XXX

(Figure 1b), and the products continuously deoxidized and eventually formed the HEAs.

As shown in Figure 1c, single-phase Cr-NF, Mo-NF, and W-NF that fit with Ni (ICDD, PDF no. 04-0850) were created by molten salt electron reduction of the oxides, which refrain from phase separation that was encountered in the conventional preparation techniques.[31] Unlike the clean surface of NF (Figure 1d), after deoxidation and reduction of oxides, HEA particles grew on NF in a coral-like form. The particle sizes of Cr-NF, Mo-NF, and W-NF are ~5 μm (Figure 1e), ~ 2.5 μm (Figure 1f), and ~400 nm (Figure 1g), respectively. To the best of our knowledge, this is the smallest-grained W-containing alloy at present.[32,33] It is worth noting that the melting points of the components are quite different (e.g., Mn 1246 °C, Cr 1907 °C, Mo 2623 °C, and W 3422 °C). The huge difference in melting point leads to the W-containing alloys being difficult to mix by the traditional arc melting method. Nevertheless, the components' decomposition voltage of the corresponding oxides is less than 1.0 V at 900 °C (Table S2). Molten $CaCl_2$ has a wide enough electrochemical window (3.231 V) to ensure the reduction of Fe_2O_3 (0.892 V), Co_3O_4 (0.596 V), NiO (0.692 V), MnO_2 (0.800 V), CrO_3 (0.537 V), MoO_2 (0.976 V), and WO_2 (0.875 V). Our experimental temperature (900 °C) is far from the melting point of the metal. After the in situ reduction, the precursor is directly transformed from a solid oxide to a solid alloy, which reduces the segregation phenomenon in the repeated melting method.

The results of SEM-EDS (Figures 1h and S3) demonstrate that the elements are distributed evenly for the Cr-NF, Mo-NF, and W-NF electrodes. Besides, the results indicate that the alloy particles attached to the nickel foam are well fused with the nickel foam, making the particles of alloys not easy to fall off. Overall, the nickel foam-based high-entropy alloys (Cr-NF, Mo-NF, and W-NF) can be obtained efficiently by molten salt electron reduction of oxides. More elemental combinations with hugely different properties can achieve a perfect fusion through this method. Moreover, the advantage of the solid-to-solid preparation progress of molten salt electrolysis will make it possible to obtain granular alloys that traditional methods cannot.

Electrocatalytic OER Performance. We evaluated the OER performances of nickel foam-based HEAs in 1.0 M KOH. As shown in Figure 2a, the W-NF electrode exhibits better oxygen evolution activity than Mo-NF, Cr-NF, NF, and many self-standing noble-metal-free OER electrodes (Tables S3 and S4, using the commercial IrO_2/Ta_2O_5−Ti electrode as a reference benchmark). The overpotentials (η) of HEAs-NF are smaller (260 mV for Cr-NF, 259 mV for Mo-NF, and 243 mV for W-NF) than that of IrO_2/Ta_2O_5−Ti (305 mV) at a lower current density (j = 10 mA cm^{-2}, Figure 2b). The W-NF electrode also only needs small overpotentials of 292 and 355 mV at high current densities of 100 and 500 mA cm^{-2}, respectively. The overpotentials are much lower than those of Cr-NF (393 and 747 mV), Mo-NF (341 and 501 mV), and IrO_2/Ta_2O_5−Ti (478 and 872 mV) at 100 and 500 mA cm^{-2}. This phenomenon indicates that W-NF has great advantages at high current density for OER.

Furthermore, the W-NF electrode also has a lower Tafel slope value (41.5 mV dec^{-1}) than Cr-NF (82.6 mV dec^{-1}), Mo-NF (70.3 mV dec^{-1}), NF (103.9 mV dec^{-1}), and IrO_2/Ta_2O_5−Ti (122.4 mV dec^{-1}), according to the Tafel plots created from the polarization curves (Figure 2c). Besides, the W-NF electrode has the largest exchange current density (j_0, Table S3). The smallest Tafel slope value and the highest exchange current density indicate that the W-NF electrode has the most favorable OER kinetics and more reactive sites than the other electrodes.

EIS results indicate that the W-NF electrode has the best conductivity (Figures 2d and S4, Table S3). The smallest semicircle of the EIS spectra and solution resistance (R_s, 0.74 Ω for W-NF, 1.17 Ω for Cr-NF, 1.05 Ω for Mo-NF, 0.91 Ω for NF, and 0.89 Ω for IrO_2/Ta_2O_5−Ti) mean that the electron-transfer kinetics for W-NF is faster. The electrochemical active surface area (ECSA) is usually utilized to assess the exposed active sites through double-layer capacitance (C_{dl}, Figure 2e). The regular shapes of the CV curves in the non-Faraday region imply the high electrical conductivity of NF-based HEAs (Figure S5).[34] As shown in Table S5, the C_{dl} values increase significantly for NF (1.54 mF cm^{-2}), Cr-NF (7.54 mF cm^{-2}), Mo-NF (9.63 mF cm^{-2}), IrO_2/Ta_2O_5−Ti (26.3 mF cm^{-2}), and W-NF (28.6 mF cm^{-2}). The corresponding ECSA values show the same trend, which are 38.5 cm^2 for NF, 188.5 cm^2 for Cr-NF, 240.8 cm^2 for Mo-NF, 657.5 cm^2 for IrO_2/Ta_2O_5−Ti, and 715.0 cm^2 for W-NF. The values of ECSA and C_{dl} confirm the OER performance of NF, Cr-NF, Mo-NF, and W-NF. Furthermore, the turnover frequency (TOF) value represents the number of transformations of a single active site per unit time of the catalyst, which indicates the intrinsic activity of the catalysts. The corresponding TOFs are 0.039 s^{-1} (NF), 0.113 s^{-1} (Cr-NF), 0.169 s^{-1} (Mo-NF), 0.227 s^{-1} (W-NF), and 0.051 s^{-1} (IrO_2/Ta_2O_5−Ti) at η = 350 mV, respectively. The TOF consequently means that the W element is beneficial for OER catalysis. The above results verify the exceptional catalytic performance of the W-NF electrode for OER.

In addition to activity, stability is another important standard for the performance of catalysts. Figure 2f shows the stability results of different electrodes by the chronopotentiometry method. Due to the dissolution of pure nickel foam at high current density, the oxygen evolution potential of nickel foam oscillates remarkably. However, the oxygen evolution stability was significantly improved after growing high-entropy alloy particles. The changed values for potential are 20.6 mV for Cr-NF, 16.1 mV for Mo-NF, 13.8 mV for W-NF, and 72.4 mV for IrO_2/Ta_2O_5−Ti after the durability test at 100 mA cm^{-2} for 5 h (Table S5). The electrodes remain in the same state as their original state (Figure S6). This result reflects the preponderance of the W-NF electrode on stability compared with other electrodes. However, in practical application, the real durability should take place at a high current density (>100 mA cm^{-2}) and a lengthy period (>50 h). As shown in Figure 2g, the W-NF electrode exhibits great catalytic durability. It shows an almost constant catalytic potential for 100 h at 10 mA cm^{-2} ($\eta \approx$ 260 mV). After that, the potential changed value after the durability test for 100 h at 100 mA cm^{-2} is only 4.7 mV ($\eta \approx$ 370 mV). Moreover, the LSV curves before and after the stability tests (Figure 2h) show a negligible reduction. The corresponding Tafel slope increases by only 5.2 mV dec^{-1} after the continuous stability test for 200 h (Figure 2i). Furthermore, under the industrialized current density (500 mA cm^{-2}), the W-NF electrode can continuously operate stably for more than 1200 h, and the overpotential changes by only 15 mV (Figure 2j). Above all, the durability test confirms the high OER stability of the W-NF electrode, which is competitive with that of the most self-standing noble-metal-free OER electrodes at high current density (Table S4).

https://doi.org/10.1021/acssuschemeng.3c04499
ACS Sustainable Chem. Eng. XXXX, XXX, XXX−XXX

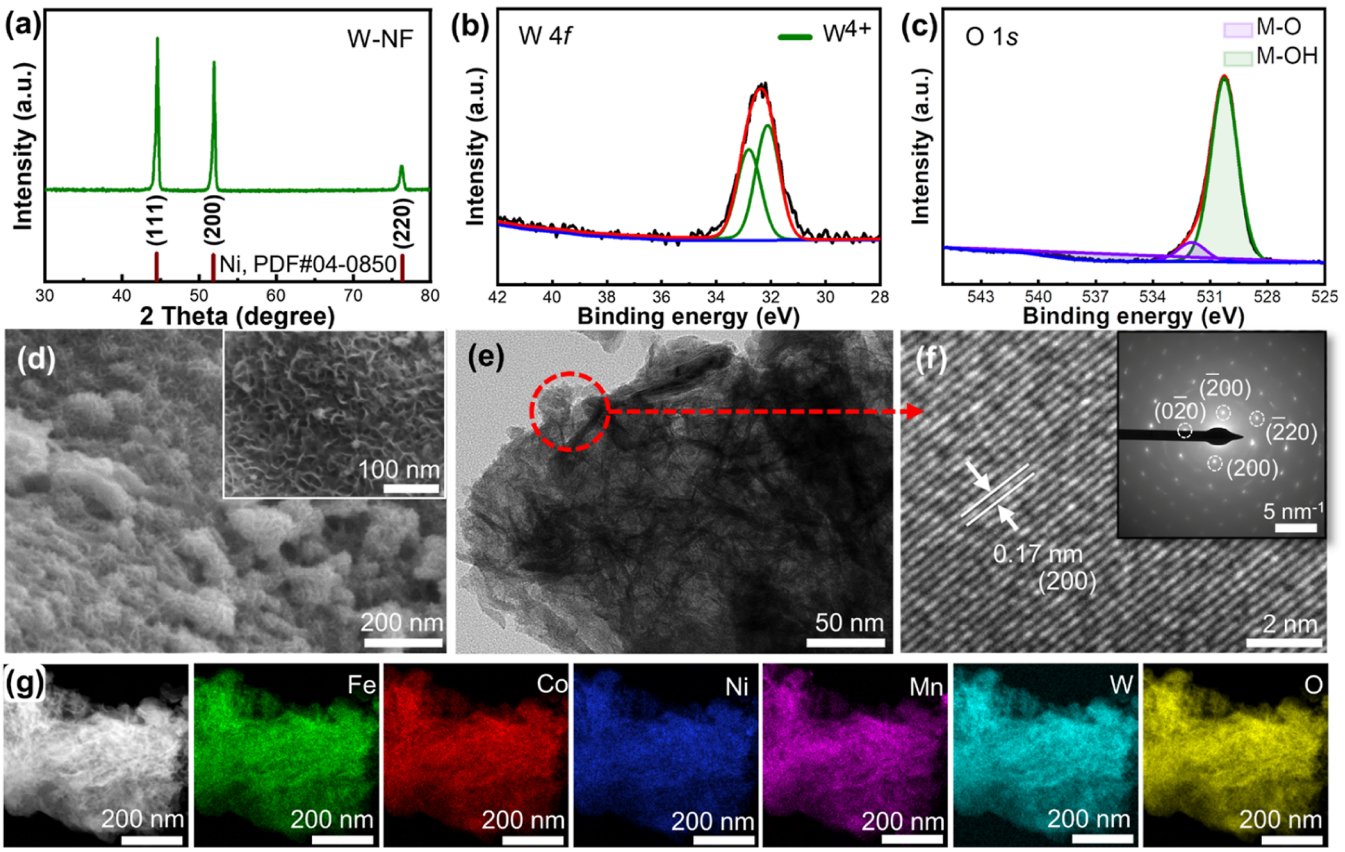

Figure 3. Surface representation of the W-NF electrode. (a) XRD pattern, (b,c) XPS spectrum, (d) SEM images, (e) HRTEM image, (f) HAADF-STEM image, and (g) EDS mapping of the W-NF electrode after durability test for continuous 1200 h at 500 mA cm^{-2}.

Surface Active Layer Investigation. The state of the active layer of the electrode is essential for catalytic performance, and systematic characterizations were performed to reveal the active layer of the NF-based HEA electrode after the stability test. The XRD patterns show that there has been no obvious change before and after the OER test (Figures 3a and S7), still maintaining the FCC phase as Ni (ICDD, PDF no. 04-0850). This may be because the oxide layer on the surface is below the limit of detection. The results of SEM prove that the distribution of the elements is still uniform after the stability test (Figure S8). In particular, the W-NF electrode showed no significant phase separation or metal loss after the 1200 h continuous stability test, which proved the excellent stability of the W-NF electrode. The W 4f spectra from W-NF (Figure 3b) indicate that the oxidation state of W is W^{4+}, and the oxidation states of Cr on Cr-NF and Mo on Mo-NF are Cr^{3+} and Mo^{6+} (Figure S9a,b), respectively, which should be the active state for OER. In addition, the O 1s spectra of Cr-NF, Mo-NF, and W-NF all show two peaks at 529.39 and 531.23 eV (Figures 3c and S9c,d),[35] which are associated with metal-oxide (M−O) bonds and metal-hydroxide (M−OH) bonds, respectively. However, the ratios of M−OH and M−O of these three electrodes are different (Table S6). The percentage of M−O bonds increases (90.2% for Cr-NF, 91.6% for Mo-NF, and 94.6% for W-NF). This means that a significant quantity of M−O bonds is advantageous for the oxygen evolution process.

Amorphous arrays grown on nickel foam is an important way to improve OER performance.[36,37] The SEM images (Figures 3d and S12a) show that the active layer is dense amorphous nano-oxide arrays on the W-NF electrode surface following the stability test. The array size is about 30 nm, which is much smaller than the arrays on the surface of Cr-NF (~150 nm, Figure S10b) and Mo-NF (~100 nm, Figure S10c). The amorphous nano-oxide arrays provide abundant active sites but also benefit the desorption of oxygen.[38,39] These phenomena are associated with the particle size of the alloys before the OER test (Figure 1e−g). In other words, the nanoparticles of W-NF provide a more compact site for forming nano-oxide arrays. The smaller arrays also verify that W-NF has the largest values of C_{dl}, ECSA, and TOF. In addition, the HRTEM images exhibit the hierarchical nano-sheet structure of the oxide layer (Figure 3e) while there are no obvious nanosheets for the oxide layers of Cr-NF (Figure S11a) and Mo-NF (Figure S12a). The HRTEM image (Figure 3f) indicates the fringes in conjunction with the selected area electron diffraction pattern. The specific lattice spacing (0.17 nm) refers to the interplanar spacing of the specific crystal plane (200) of FeCoNiMnW HEA. In comparison, the lattice spacing of the lattice fringes of Cr-NF and Mo-NF are both ~0.2 nm, representing the (211) crystal plane (Figures S11b and S12b). It is worth noting that, unlike the diffraction spots of a cubic system of W-MF and Mo-NF (Figures 3f and S12c), the diffraction spots of Cr-NF are polycrystalline structures (Figure S11c). This may be due to the phase separation of the selected part after oxygen evolution. Furthermore, the TEM-EDS images (Figures 3g, S11d and S12d) confirm the generation of the HEA oxide layer, and the oxidation occurs uniformly on all elements. These phenomena prove that the refractory metals (Mo and W) promote stability of the

https://doi.org/10.1021/acssuschemeng.3c04499
ACS Sustainable Chem. Eng. XXXX, XXX, XXX−XXX

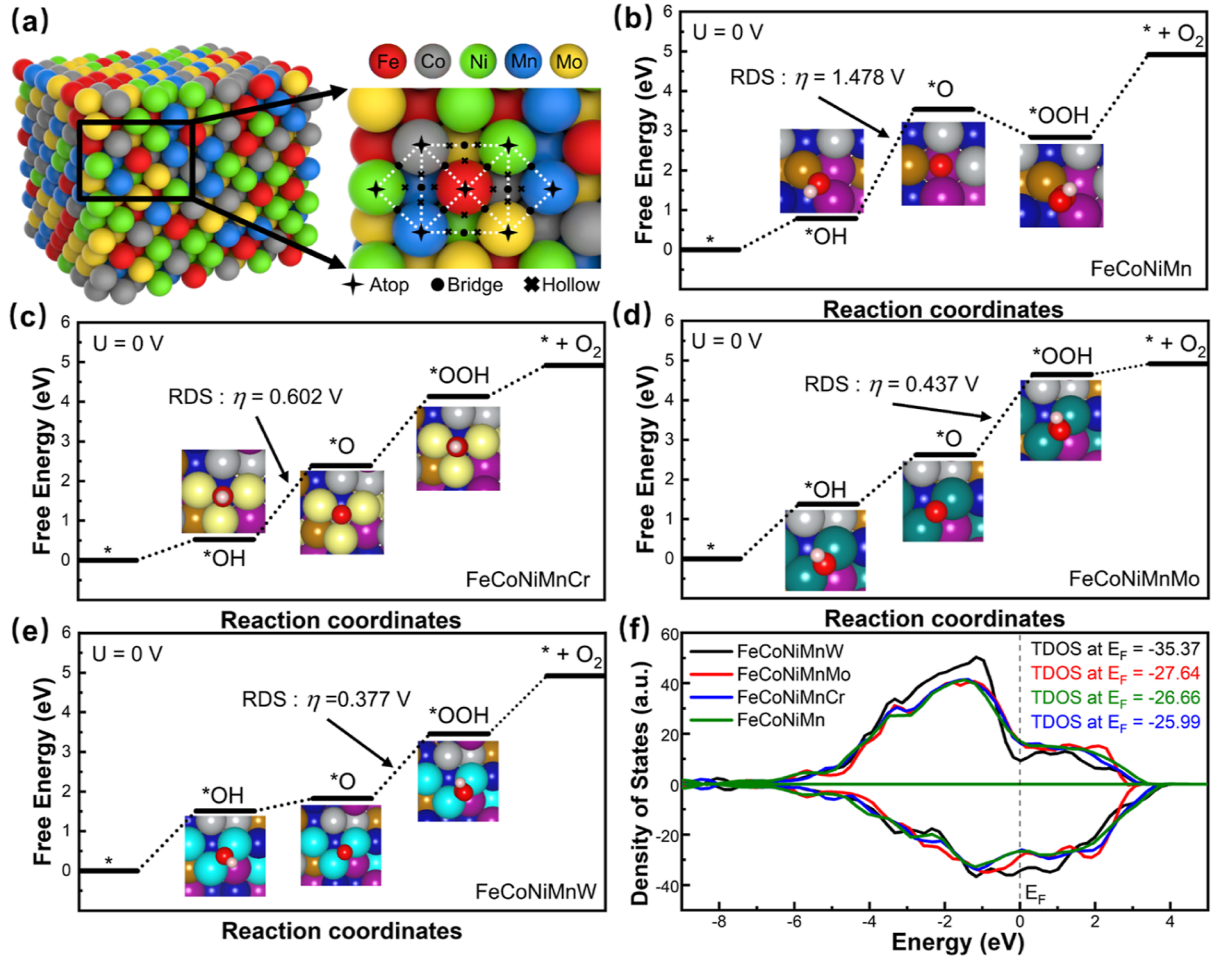

Figure 4. Theoretical calculation of the electrodes for the OER. (a) Diagrams of different active sites (atop, bridge, hollow) in high-entropy alloys. The free-energy landscape at 0 V for (b) FeCoNiMn, (c) FeCoNiMnCr, (d) FeCoNiMnMo, and (e) FeCoNiMnW electrodes. (f) TDOS plots for different electrodes.

structure of the HEAs. These results demonstrate the feasibility of preparing HEAs using the molten salt electrolytic reduction method and their excellent stability when used for OER.

First-Principles Calculations of Active Sites for High-Entropy Alloys. The theoretical calculation is beneficial for revealing the active sites of high-entropy alloys. Combining the conventional adsorbate evolution mechanism (AEM, Figure S13),[40,41] the theoretical calculation can give a profound interpretation of the mechanism of a multicomponent system for OER. We considered the different active sites at atop, bridge, and hollow (Figure 4a) positions; all theoretical results show that the system energy is the lowest when the oxygen-containing substances are adsorbed at the bridge sites.

To reveal the effect of Cr, Mo, and W addition on the OER performance, we computed the energy barriers during the OER process of FeCoNiMn, FeCoNiMnCr, FeCoNiMnMo, and FeCoNiMnW based on the most stable model. Taking the adsorption of *O on FeCoNiMn (Figure S14), FeCoNiMnCr (Figure S15), FeCoNiMnMo (Figure S16), and FeCoNiMnW (Figure S17) as examples, we considered 16 types of models to determine the optimal adsorption sites. Among them, Type 3 is the most stable model of system energy (−225.986 eV for FeCoNiMn, −240.183 eV for FeCoNiMnCr, −249.220 eV for FeCoNiMnMo, and −261.995 eV for FeCoNiMnW). The results show that the multiactive bridge sites on Cr, Mo, or W are the most superior adsorption configurations, reducing the energy required during the OER process. Furthermore, we can see the models' change before and after the OER calculations process (with the adsorption of *OH, *O, and *OOH) of FeCoNiMn (Figure S18), FeCoNiMnCr (Figure S19), FeCoNiMnMo (Figure S20), and FeCoNiMnW (Figure S21). The optimized models demonstrated suitable active sites, adsorption energies, and intrinsic activity. From the free-energy landscapes at 0 V, we can extrapolate that the rate-determining step (RDS) for FeCoNiMn and FeCoNiMnCr is the step from M-*OH to M-*O. However, the step from M-*O to M-*OOH acts as the RDS for FeCoNiMnMo and FeCoNiMnW. The corresponding overpotential (η) derived from the RDS is 1.487 V for FeCoNiMn (Figure 4b), 0.602 V for FeCoNiMnCr (Figure 4c), 0.437 V for FeCoNiMnMo (Figure 4d), and 0.377 V for FeCoNiMnW (Figure 4e). Therefore, the addition of Cr, Mo, and W elements based on the quaternary alloy (FeCoNiMn) greatly weakens the overpotential of the RDS in the OER process. The experimental results of the law of the overpotential are consistent with the conclusions of the theoretical calculation. Moreover, the theoretical overpotential of FeCoNiMnW is close to that of high-entropy alloys containing noble metals. This result further verifies the advantages of the noble-metal-free FeCoNiMnW-NF electrode as an OER catalyst.

Figure 4f shows the total density of states (TDOS) of the FeCoNiMn, FeCoNiMnCr, FeCoNiMnMo, and FeCoNiMnW

https://doi.org/10.1021/acssuschemeng.3c04499
ACS Sustainable Chem. Eng. XXXX, XXX, XXX−XXX

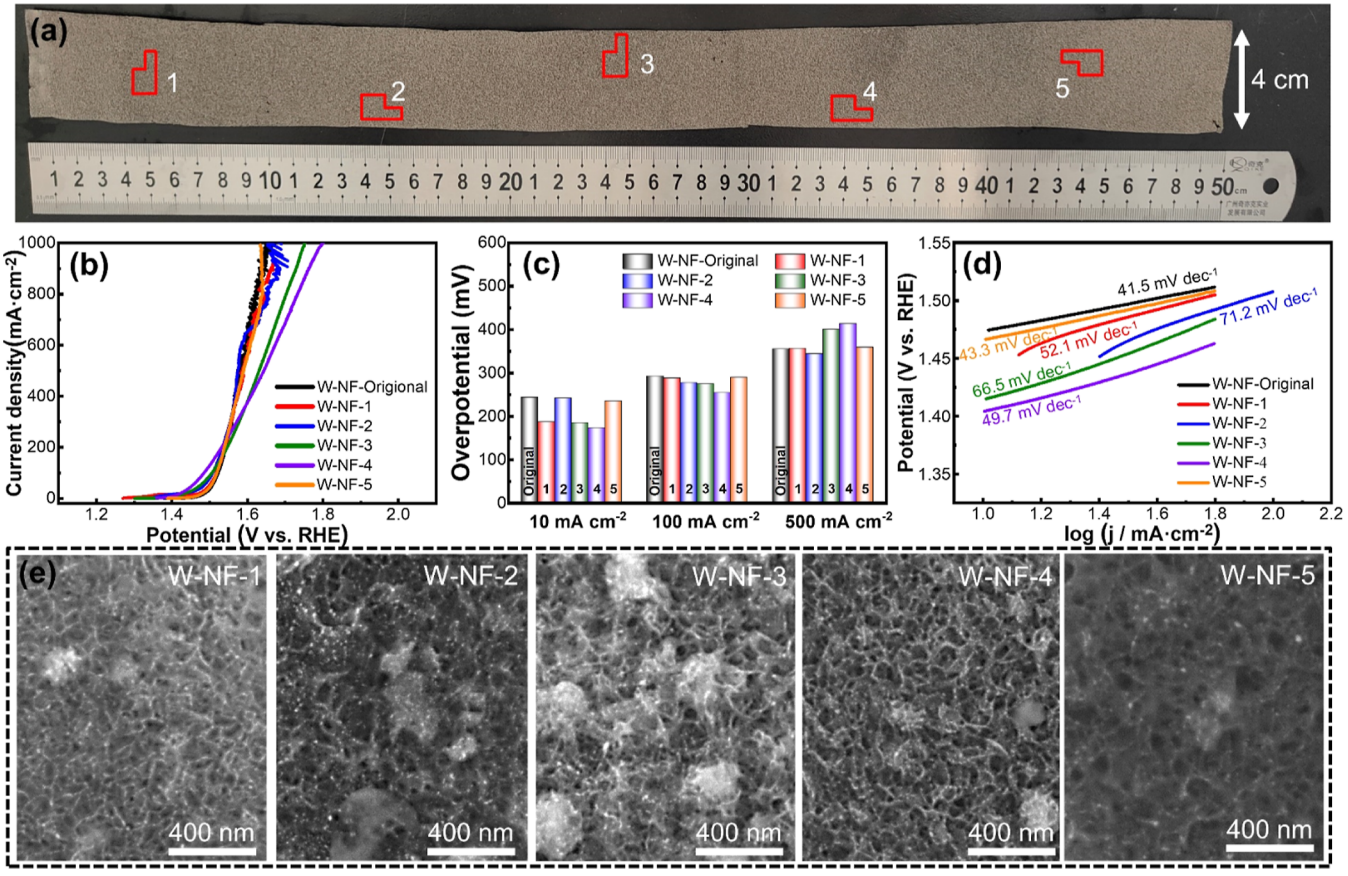

Figure 5. Scale-up experiments of the W-NF electrode. (a) Digital graph of the W-NF electrode for the scale of 40 × 500 mm. (b) LSV curves, (c) overpotentials at 10, 100, and 500 mA cm^{-2}, (d) Tafel plots, and (e) SEM images of representative areas 1−5 in the scale-up electrode.

electrodes. It can be seen that the TDOS values of the electrodes at the Fermi level are larger than 0, and the order of TDOS at the Fermi level from large to small is FeCoNiMnW, FeCoNiMnMo, FeCoNiMnCr, FeCoNiMn. The result indicates that these electrodes are excellent conductors with abundant electrons and fast electron-transport speeds for OER.[42] The corresponding spin-dependent projected density of states (PDOS, Figure S22) further reveals the electronic environment of the electrodes. The results show that for all electrodes, the d-orbital almost coincides with the DOS of the corresponding elements, and the p-orbital and s-orbital almost have no effect. This means that transition-metal electrodes play an oxygen evolution role mainly by electrons in the d-orbital. In addition, for the FeCoNiMn electrode, the position of *d*-band centers of Ni occupied a larger position away from the Fermi level (Figure S22a), which means that Ni is an important element in the process of OER.[43] Unlike the quaternary alloy, with the addition of Cr (Figure S22b), Mo (Figure S22c), and W (Figure S22d), the effect of Ni decreases. However, the TDOS of the system increased, indicating that the synergistic effect of the HEAs helps the electrodes in playing a better catalytic role.

Scale-up Experiment. The previous contents have proven the excellent OER performance of the FeCoNiMnW-NF electrode under laboratory conditions. Still, large-scale electrodes are needed for practical applications. To verify the application of the FeCoNiMnW-NF electrode on a large scale, a scale-up electrode (40 × 500 mm, Figure 5a) was prepared for the OER test. We randomly selected 5 areas (the effective areas of areas 1−5 are 10 mm × 10 mm, named W-NF-1 to 5). The LSV polarization curves (Figure 5b) and overpotentials (Figure 5c) of representative W-NF electrodes prove that the electrodes have similar OER activity as the original small-scale W-NF electrode (Figure S6). In addition, the corresponding Tafel slope values (Figure 5d) are larger (52.1 mV dec^{-1} for W-NF-1, 71.2 mV dec^{-1} for W-NF-2, 66.5 mV dec^{-1} for W-NF-3, 49.7 mV dec^{-1} for W-NF-4, and 43.3 mV dec^{-1} for W-NF-5) than the original small-scale electrode (Figure S6). This may be due to the uneven distribution of oxides supported on the large-sized nickel foam (Figure S23). In addition, we characterized the surface oxide layer of the representative electrodes W-NF-1 to 5 after the electrochemical tests (Figure 5e). The results show similar amorphous nano-oxide arrays to the original W-NF electrode (Figure 3d). The above results demonstrate that the FeCoNiMnW-NF electrode can be prepared at a low cost and fast speed by one-step molten salt electrolysis and applied for industrial OER catalysis.

CONCLUSIONS

In summary, a series of pure FeCoNiMnX HEAs were prepared in only a one-step molten salt electrolysis for just 900 s (at 900 °C). The particle size of HEAs was determined by the melting point of X. FeCoNiMnW with a 400 nm particle size shows the best OER activity (η = 355 mV at 500 mA cm^{-2}) and stability (continued 50 days at 500 mA cm^{-2} with tiny changes of overpotential). The amorphous nano-oxide arrays on the surface of the electrode (~30 nm), low solution resistance (0.74 Ω), and high ECSA (715.0 cm^2) and

https://doi.org/10.1021/acssuschemeng.3c04499
ACS Sustainable Chem. Eng. XXXX, XXX, XXX−XXX

TOF (0.227 s^{-1}) of the FeCoNiMnW-NF electrode supported the high effectiveness of the OER performance. First-principles calculations indicate the excellent catalytic performance of FeCoNiMnW thanks to the largest TDOS which accelerates the electrons' transport speed for OER. Furthermore, a large electrode coated with FeCoNiMnW (40 mm × 500 mm) with similar OER performance suggests the scalability of this rapid electrochemical method. More importantly, this paper offers a general electrochemical method to synthesize various single-phase HEAs with favorable functionalities.

■ ASSOCIATED CONTENT

Supporting Information

The Supporting Information is available free of charge at https://pubs.acs.org/doi/10.1021/acssuschemeng.3c04499.

More details of computational and preparation methods, characterization results, DFT models, and data statistics (PDF)

■ AUTHOR INFORMATION

Corresponding Authors

Huayi Yin − *International Cooperation Base for Sustainable Utilization of Resources and Energy, Wuhan University, Wuhan 430072 Hubei, China; School of Resource and Environmental Science, Wuhan University, Wuhan 430072 Hubei, China*; Email: yinhuayi@whu.edu.cn

Dihua Wang − *International Cooperation Base for Sustainable Utilization of Resources and Energy, Wuhan University, Wuhan 430072 Hubei, China; School of Resource and Environmental Science, Wuhan University, Wuhan 430072 Hubei, China*; orcid.org/0000-0003-2364-8718; Email: wangdh@whu.edu.cn

Authors

Peng Li − *International Cooperation Base for Sustainable Utilization of Resources and Energy, Wuhan University, Wuhan 430072 Hubei, China; School of Resource and Environmental Science, Wuhan University, Wuhan 430072 Hubei, China; School of Energy and Power Engineering, North University of China, Taiyuan 030051 Shanxi, China*; orcid.org/0000-0001-7828-5876

Bozhao Wu − *Department of Engineering Mechanics, School of Civil Engineering, Wuhan University, Wuhan 430072 Hubei, China*

Kaifa Du − *International Cooperation Base for Sustainable Utilization of Resources and Energy, Wuhan University, Wuhan 430072 Hubei, China; School of Resource and Environmental Science, Wuhan University, Wuhan 430072 Hubei, China*

Ze Liu − *Department of Engineering Mechanics, School of Civil Engineering, Wuhan University, Wuhan 430072 Hubei, China*

Enlai Gao − *Department of Engineering Mechanics, School of Civil Engineering, Wuhan University, Wuhan 430072 Hubei, China*

Complete contact information is available at: https://pubs.acs.org/10.1021/acssuschemeng.3c04499

Notes

The authors declare no competing financial interest.

■ ACKNOWLEDGMENTS

The authors thank National Natural Science Foundation of China (nos. 52031008, 12172260), and the Key Research and Development Program of Hubei Province (no. 2021BAA192) for the funding.

■ REFERENCES

(1) Zhang, B.; Zheng, X.; Voznyy, O.; Comin, R.; Bajdich, M.; García-Melchor, M.; Han, L.; Xu, J.; Liu, M.; Zheng, L.; García de Arquer, F. P.; Dinh, C. T.; Fan, F.; Yuan, M.; Yassitepe, E.; Chen, N.; Regier, T.; Liu, P.; Li, Y.; De Luna, P.; Janmohamed, A.; Xin, H. L.; Yang, H.; Vojvodic, A.; Sargent, E. H. Homogeneously Dispersed Multimetal Oxygen-Evolving Catalysts. *Science* **2016**, *352* (6283), 333−337.

(2) Yao, Y.; Dong, Q.; Brozena, A.; Luo, J.; Miao, J.; Chi, M.; Wang, C.; Kevrekidis, I. G.; Ren, Z. J.; Greeley, J.; Wang, G.; Anapolsky, A.; Hu, L. High-Entropy Nanoparticles: Synthesis-Structure-Property Relationships and Data-Driven Discovery. *Science* **2022**, *376* (6589), No. eabn3103, DOI: 10.1126/science.abn3103.

(3) Li, J. Oxygen Evolution Reaction in Energy Conversion and Storage: Design Strategies Under and Beyond the Energy Scaling Relationship. *Nanomicro. Lett.* **2022**, *14* (1), 112.

(4) Jiang, B.; Xue, H.; Wang, P.; Du, H.; Kang, Y.; Zhao, J.; Wang, S.; Zhou, W.; Bian, Z.; Li, H.; Henzie, J.; Yamauchi, Y. Noble-Metal−Metalloid Alloy Architectures: Mesoporous Amorphous Iridium−Tellurium Alloy for Electrochemical N_2 Reduction. *J. Am. Chem. Soc.* **2023**, *145* (11), 6079−6086.

(5) Wang, J.; Yang, H.; Li, F.; Li, L.; Wu, J.; Liu, S.; Cheng, T.; Xu, Y.; Shao, Q.; Huang, X. Single-Site Pt-Doped RuO_2 Hollow Nanospheres with Interstitial C for High-Performance Acidic Overall Water Splitting. *Sci. Adv.* **2022**, *8* (9), 9271.

(6) Xiang, W.; Yang, N.; Li, X.; Linnemann, J.; Hagemann, U.; Ruediger, O.; Heidelmann, M.; Falk, T.; Aramini, M.; DeBeer, S.; Muhler, M.; Tschulik, K.; Li, T. 3D Atomic-Scale Imaging of Mixed Co-Fe Spinel Oxide Nanoparticles during Oxygen Evolution Reaction. *Nat. Commun.* **2022**, *13* (1), 179.

(7) Cao, Z.; Zhou, T.; Ma, X.; Shen, Y.; Deng, Q.; Zhang, W.; Zhao, Y. Hydrogen Production from Urea Sewage on NiFe-Based Porous Electrocatalysts. *ACS Sustain. Chem. Eng.* **2020**, *8*, 11007−11015.

(8) Dionigi, F.; Zeng, Z.; Sinev, I.; Merzdorf, T.; Deshpande, S.; Lopez, M. B.; Kunze, S.; Zegkinoglou, I.; Sarodnik, H.; Fan, D.; Bergmann, A.; Drnec, J.; de Araujo, J. F.; Gliech, M.; Teschner, D.; Zhu, J.; Li, W. X.; Greeley, J.; Cuenya, B. R.; Strasser, P. In-Situ Structure and Catalytic Mechanism of NiFe and CoFe Layered Double Hydroxides during Oxygen Evolution. *Nat. Commun.* **2020**, *11* (1), 2522.

(9) Zhang, J.; Liu, J.; Zhang, L.; Ke, J.; Zhong, C.; Tu, Y.; Wang, L.; Song, H.; Du, L.; Zhang, Z.; Cui, Z. Fe^{3+}-Preactivated Ni/Co-Based Antiperovskite Nitrides for Boosting Oxygen Evolution: Surface Tuning and Catalytic Mechanism. *ACS Catal.* **2023**, *13* (7), 5043−5052.

(10) Menezes, P. W.; Panda, C.; Walter, C.; Schwarze, M.; Driess, M. A Cobalt-Based Amorphous Bifunctional Electrocatalysts for Water-Splitting Evolved from a Single-Source Lazulite Cobalt Phosphate. *Adv. Funct. Mater.* **2019**, *29* (32), 1808632.

(11) Qiao, H.; Wang, X.; Dong, Q.; Zheng, H.; Chen, G.; Hong, M.; Yang, C. P.; Wu, M.; He, K.; Hu, L. A High-Entropy Phosphate Catalyst for Oxygen Evolution Reaction. *Nano Energy* **2021**, *86*, 106029.

(12) Singh, S.; Wanderka, N.; Murty, B. S.; Glatzel, U.; Banhart, J. Decomposition in Multi-Component AlCoCrCuFeNi High-Entropy Alloy. *Acta Mater.* **2011**, *59* (1), 182−190.

(13) Wu, D.; Kusada, K.; Yamamoto, T.; Toriyama, T.; Matsumura, S.; Gueye, I.; Seo, O.; Kim, J.; Hiroi, S.; Sakata, O.; Kawaguchi, S.; Kubota, Y.; Kitagawa, H. On the Electronic Structure and Hydrogen Evolution Reaction Activity of Platinum Group Metal-Based High-Entropy-Alloy Nanoparticles. *Chem. Sci.* **2020**, *11* (47), 12731−12736.

(14) Yang, H.; Gong, L.; Wang, H.; Dong, C.; Wang, J.; Qi, K.; Liu, H.; Guo, X.; Xia, B. Y. Preparation of Nickel-Iron Hydroxides by Microorganism Corrosion for Efficient Oxygen Evolution. *Nat. Commun.* **2020**, *11* (1), 5075.
(15) Schäfer, H.; Sadaf, S.; Walder, L.; Kuepper, K.; Dinklage, S.; Wollschläger, J.; Schneider, L.; Steinhart, M.; Hardege, J.; Daum, D. Stainless Steel Made to Rust: A Robust Water-Splitting Catalyst with Benchmark Characteristics. *Energy Environ. Sci.* **2015**, *8* (9), 2685−2697.
(16) Wei, L.; Liu, X.; Gao, Y.; Peng, X.; Hu, N.; Chen, M. Phase, Microstructure and Mechanical Properties Evaluation of AlCoCrFeNi High-Entropy Alloy during Mechanical Ball Milling. *Intermetallics* **2021**, *138*, 107310.
(17) Jiang, L.; Hu, Y. J.; Sun, K.; Xiu, P.; Song, M.; Zhang, Y.; Boldman, W. L.; Crespillo, M. L.; Rack, P. D.; Qi, L.; Weber, W. J.; Wang, L. Irradiation-Induced Extremes Create Hierarchical Face-/Body-Centered-Cubic Phases in Nanostructured High Entropy Alloys. *Adv. Mater.* **2020**, *32* (39), 2002652.
(18) Bondesgaard, M.; Broge, N. L. N.; Mamakhel, A.; Bremholm, M.; Iversen, B. B. General Solvothermal Synthesis Method for Complete Solubility Range Bimetallic and High-Entropy Alloy Nanocatalysts. *Adv. Funct. Mater.* **2019**, *29* (50), 1905933.
(19) Gao, S.; Hao, S.; Huang, Z.; Yuan, Y.; Han, S.; Lei, L.; Zhang, X.; Shahbazian-Yassar, R.; Lu, J. Synthesis of High-Entropy Alloy Nanoparticles on Supports by the Fast Moving Bed Pyrolysis. *Nat. Commun.* **2020**, *11* (1), 2016.
(20) Kang, Y.; Cretu, O.; Kikkawa, J.; Kimoto, K.; Nara, H.; Nugraha, A. S.; Kawamoto, H.; Eguchi, M.; Liao, T.; Sun, Z.; Asahi, T.; Yamauchi, Y. Mesoporous Multimetallic Nanospheres with Exposed Highly Entropic Alloy Sites. *Nat. Commun.* **2023**, *14* (1), 4182.
(21) George, E. P.; Raabe, D.; Ritchie, R. O. High-Entropy Alloys. *Nat. Rev. Mater.* **2019**, *4* (8), 515−534.
(22) Ahn, J.; Park, S.; Oh, D.; Lim, Y.; Nam, J. S.; Kim, J.; Jung, W.; Kim, I.-D. Rapid Joule Heating Synthesis of Oxide-Socketed High-Entropy Alloy Nanoparticles as CO_2 Conversion Catalysts. *ACS Nano* **2023**, *17* (13), 12188−12199.
(23) Xu, X. D.; Liu, P.; Guo, S.; Hirata, A.; Fujita, T.; Nieh, T. G.; Liu, C. T.; Chen, M. W. Nanoscale Phase Separation in a Fcc-Based $CoCrCuFeNiAl_{0.5}$ High-Entropy Alloy. *Acta Mater.* **2015**, *84*, 145−152.
(24) Minamihara, H.; Kusada, K.; Wu, D.; Yamamoto, T.; Toriyama, T.; Matsumura, S.; Kumara, L. S. R.; Ohara, K.; Sakata, O.; Kawaguchi, S.; Kubota, Y.; Kitagawa, H. Continuous-Flow Reactor Synthesis for Homogeneous 1 nm-Sized Extremely Small High-Entropy Alloy Nanoparticles. *J. Am. Chem. Soc.* **2022**, *144* (26), 11525−11529.
(25) Yao, Y.; Huang, Z.; Xie, P.; Lacey, S. D.; Jacob, R. J.; Xie, H.; Chen, F.; Nie, A.; Pu, T.; Rehwoldt, M.; Yu, D.; Zachariah, M. R.; Wang, C.; Shahbazian-Yassar, R.; Li, J.; Hu, L. Carbothermal Shock Synthesis of High-Entropy-Alloy Nanoparticles. *Science* **2018**, *359* (6383), 1489−1494.
(26) Kresse, G.; Furthmüller, J. Efficient Iterative Schemes for Ab Initio Total-Energy Calculations Using a Plane-Wave Basis Set. *Phys. Rev. B: Condens. Matter Mater. Phys.* **1996**, *54* (16), 11169−11186.
(27) Kresse, G.; Joubert, D. From Ultrasoft Pseudopotentials to the Projector Augmented-Wave Method. *Phys. Rev. B: Condens. Matter Mater. Phys.* **1999**, *59* (3), 1758−1775.
(28) Perdew, J. P.; Burke, K.; Ernzerhof, M. Generalized Gradient Approximation Made Simple. *Phys. Rev. Lett.* **1996**, *77* (18), 3865−3868.
(29) Filippi, C.; Singh, D. J.; Umrigar, C. J. All-Electron Local-Density and Generalized-Gradient Calculations of the Structural Properties of Semiconductors. *Phys. Rev. B: Condens. Matter Mater. Phys.* **1994**, *50* (20), 14947−14951.
(30) Monkhorst, H. J.; Pack, J. D. Special Points for Brillouin-Zone Integrations. *Phys. Rev. B: Solid State* **1976**, *13* (12), 5188−5192.
(31) Guo, T.; Li, J.; Wang, J.; Wang, Y.; Kou, H.; Niu, S. Liquid-Phase Separation in Undercooled CoCrCuFeNi High Entropy Alloy. *Intermetallics* **2017**, *86*, 110−115.
(32) Li, Q.; Zhang, H.; Li, D.; Chen, Z.; Huang, S.; Lu, Z.; Yan, H. $W_xNbMoTa$ Refractory High-Entropy Alloys Fabricated by Laser Cladding Deposition. *Materials* **2019**, *12* (3), 533.
(33) Samin, A. J. A Computational Investigation of the Interstitial Oxidation Thermodynamics of a Mo-Nb-Ta-W High Entropy Alloy beyond the Dilute Regime. *J. Appl. Phys.* **2020**, *128* (21), 215101.
(34) Ge, R.; Huo, J.; Liao, T.; Liu, Y.; Zhu, M.; Li, Y.; Zhang, J.; Li, W. Hierarchical Molybdenum Phosphide Coupled with Carbon as a Whole PH-Range Electrocatalyst for Hydrogen Evolution Reaction. *Appl. Catal., B* **2020**, *260*, 118196.
(35) Zhou, P.; Niu, P.; Liu, J.; Zhang, N.; Bai, H.; Chen, M.; Feng, J.; Liu, D.; Wang, L.; Chen, S.; Kwok, C. T.; Tang, Y.; Li, R.; Wang, S.; Pan, H. Anodized Steel: The Most Promising Bifunctional Electrocatalyst for Alkaline Water Electrolysis in Industry. *Adv. Funct. Mater.* **2022**, *32* (26), 2202068.
(36) Jiang, Z.-Q.; Chen, X.-L.; Fan, W.-J.; Jiang, W.-D.; Li, Y.-F.; Zhang, D.-X.; Wen, T. Mn_{13}-Cluster-Based Nanowire Arrays Deposited on Ni Foam for the Oxygen Evolution Reaction. *ACS Appl. Nano Mater.* **2022**, *5* (1), 326−330.
(37) Hu, Y.; Wang, Z.; Liu, W.; Xu, L.; Guan, M.; Huang, Y.; Zhao, Y.; Bao, J.; Li, H. Novel Cobalt−Iron−Vanadium Layered Double Hydroxide Nanosheet Arrays for Superior Water Oxidation Performance. *ACS Sustain. Chem. Eng.* **2019**, *7* (19), 16828−16834.
(38) Huang, H.; Li, J. R.; Wang, K.; Han, T.; Tong, M.; Li, L.; Xie, Y.; Yang, Q.; Liu, D.; Zhong, C. An in Situ Self-Assembly Template Strategy for the Preparation of Hierarchical-Pore Metal-Organic Frameworks. *Nat. Commun.* **2015**, *6* (1), 8847.
(39) Zhang, C.; Huang, Y.; Yu, Y.; Zhang, J.; Zhuo, S.; Zhang, B. Sub-1.1 Nm Ultrathin Porous CoP Nanosheets with Dominant Reactive {200} Facets: A High Mass Activity and Efficient Electrocatalyst for the Hydrogen Evolution Reaction. *Chem. Sci.* **2017**, *8* (4), 2769−2775.
(40) Zhang, L.; Cai, W.; Bao, N.; Yang, H. Implanting an Electron Donor to Enlarge the d−p Hybridization of High-Entropy (Oxy)-Hydroxide: A Novel Design to Boost Oxygen Evolution. *Adv. Mater.* **2022**, *34* (26), 2110511.
(41) Pan, Y.; Xu, X.; Zhong, Y.; Ge, L.; Chen, Y.; Veder, J. P. M.; Guan, D.; O'Hayre, R.; Li, M.; Wang, G.; Wang, H.; Zhou, W.; Shao, Z. Direct Evidence of Boosted Oxygen Evolution over Perovskite by Enhanced Lattice Oxygen Participation. *Nat. Commun.* **2020**, *11* (1), 2002.
(42) Zhang, L.; Cai, W.; Bao, N. Top-Level Design Strategy to Construct an Advanced High-Entropy Co−Cu−Fe−Mo (Oxy)-Hydroxide Electrocatalyst for the Oxygen Evolution Reaction. *Adv. Mater.* **2021**, *33* (22), 21100745.
(43) Wang, S.; Huo, W.; Fang, F.; Xie, Z.; Shang, J. K.; Jiang, J. High Entropy Alloy/C Nanoparticles Derived from Polymetallic MOF as Promising Electrocatalysts for Alkaline Oxygen Evolution Reaction. *Chem. Eng. J.* **2022**, *429*, 132410.

https://doi.org/10.1021/acssuschemeng.3c04499
ACS Sustainable Chem. Eng. XXXX, XXX, XXX−XXX

Supporting Information

Highly Stable Single-phase FeCoNiMnX (X=Cr, Mo, W) High-Entropy Alloy Catalysts with Submicrometer Size for Efficient Oxygen Evolution

Peng Li,[1,2,4] Bozhao Wu,[3] Kaifa Du,[1,2] Ze Liu,[3] Enlai Gao,[3] Huayi Yin,[1,2,*] Dihua Wang[1,2,*]

1) International Cooperation Base for Sustainable Utilization of Resources and Energy, Wuhan University, Wuchang District, No. 299 Bayi Road, Wuhan 430072, Hubei, China
2) School of Resource and Environmental Science, Wuhan University, Wuchang District, No. 299 Bayi Road, Wuhan 430072, Hubei, China
3) Department of Engineering Mechanics, School of Civil Engineering, Wuhan University, Wuchang District, No. 299 Bayi Road, Wuhan 430072, Hubei, China
4) School of Energy and Power Engineering, North University of China, Jiancaoping District, No. 3 Xueyuan Road, Taiyuan 030051, Shanxi, China

*Corresponding author:

Huayi Yin – E-mail address:yinhuayi@whu.edu.cn

Dihua Wang – E-mail address: wangdh@whu.edu.cn

Number of Pages: 29

Number of Figures: 23

Number of Tables: 6

Table of Contents

1. Supporting Methods

1.1 Calculation method of exchange current density (j_0)[1,2]

Tafel analysis is usually employed to indicate the reaction kinetics and catalytic activity. The Tafel slope helps to define the rate-determining step by the following equation :

$$\eta = b \log j + a \quad \text{(S1)}$$

Where the η is overpotential (V), j is the current density (mA cm^{-2}), and b is the Tafel slope value (mV dec^{-1}).

The exchange current density (j_0, mA cm^{-2}) is the corresponding value of j when η = 0 V. Low Tafel slope and large current density are the standards for a good OER catalyst. The smaller value of the Tafel slope of the reaction indicates that the activation energy required for the reaction is lower and the reaction is faster.

1.2 Calculation method of electrochemical active surface area (ECSA)[3]

The electrochemical active surface area (ECSA) can be used to estimate exposed active sites by the double-layer capacitances (C_{dl}). The calculation equation is as follows:

$$\text{ECSA} = C_{dl} / C_s \quad \text{(S2)}$$

Where C_{dl} is tested by cyclic voltammetry at different scan rates (10, 20, 30, 40, and 50 mV s^{-1}) in non-Fradic potential, C_s is the specific capacitance of the corresponding smooth surface sample (0.04 mF cm^{-2}).

1.3 Calculation method of turnover frequency (TOF)[4,5]

The turnover frequency (TOF) is an intrinsic property and an important indicator of the catalyst performance. The calculation equation is as follows:

$$\text{TOF} = (j \times a) / (4 \times n \times F) \quad \text{(S3)}$$

Where j is the current density at a specified voltage, a is the electrodes' surface area, and F is the Faraday constant (96485 C mol^{-1}).

1.4 The conventional adsorbate evolution mechanism (AEM)[6,7]

$$2H_2O + {}^{*} \rightarrow {}^{*}OH + H_2O + H^{+} + e^{-} \quad \text{(S4)}$$

$${}^{*}OH + H_2O + H^{+} + e^{-} \rightarrow {}^{*}O + H_2O + 2(H^{+} + e^{-}) \quad \text{(S5)}$$

$${}^{*}O + H_2O + 2(H^{+} + e^{-}) \rightarrow {}^{*}OOH + 3(H^{+} + e^{-}) \quad \text{(S6)}$$

$${}^{*}OOH + 3(H^{+} + e^{-}) \rightarrow O_2 + 4(H^{+} + e^{-}) \quad \text{(S7)}$$

Where * is the active site.

1.5 Calculation method of theoretical overpotential by free energy

$$\eta = \frac{\max\{\Delta G_1, \Delta G_2, \Delta G_3, \Delta G_4\}}{e} - 1.23\ \text{V} \quad \text{(S8)}$$

Where η is the theoretical overpotential. ΔG_1, ΔG_2, ΔG_3, and ΔG_4 are the Gibbs free energy of reactions (S4), (S5), (S6), and (S7), respectively.

2. Supporting Figures

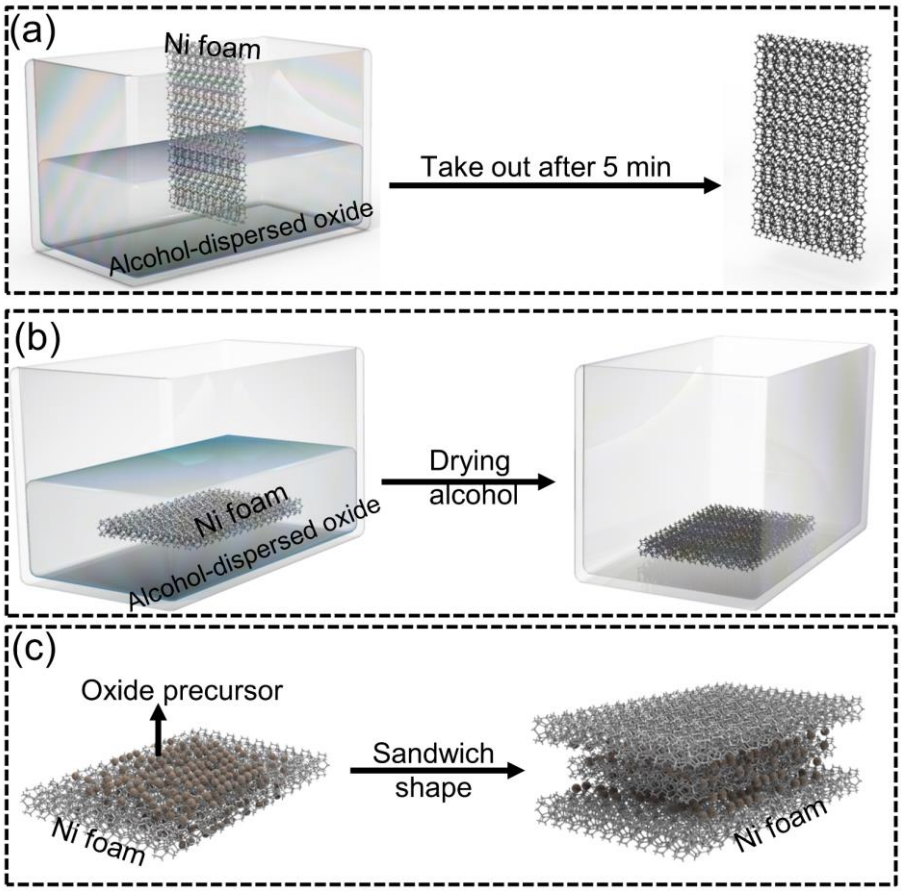

Figure S1. Three methods for the oxide coating on the Ni foam. put the Ni foam (10 mm ×10 mm × 1 mm) into the dispersions for 5 min (a), or until the alcohol dried (b). Put the oxide mixture on the nickel foam and wrap it into a sandwich shape with fresh nickel foam (c).

Figure S2. The optical photo of the bottom of the electrolyte after polarization test of products prepared by sandwich shape (Figure S1c).

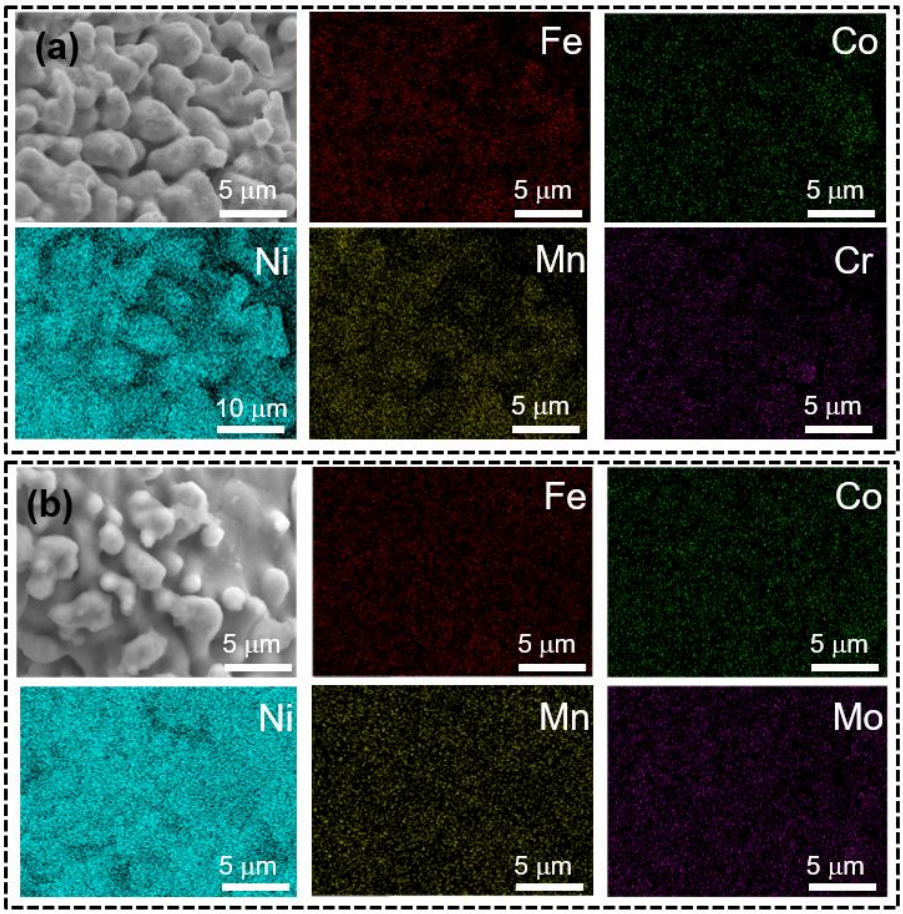

Figure S3. SEM-EDS images of Cr-NF (a) and Mo-NF (b) electrodes before the OER test.

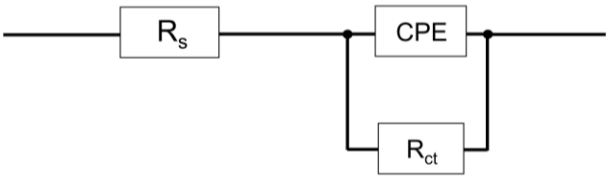

Figure S4. The equivalent circuit of the electrochemical impedance spectroscopy (EIS). R_{ct}: charge transfer resistance; R_s: solution resistance; CPE: constant phase element.

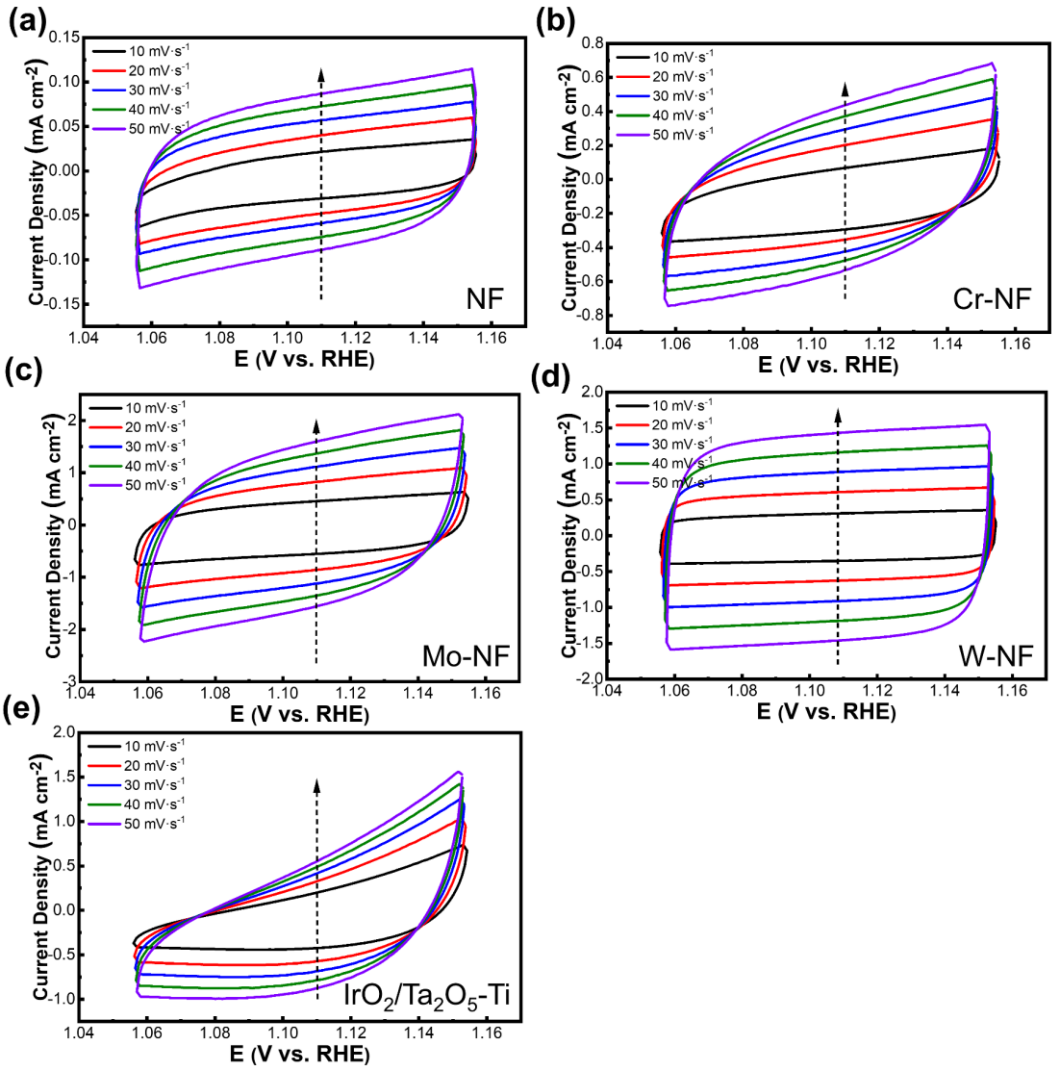

Figure S5. CV curves of NF (a), Cr-NF (b), Mo-NF (c), W-NF (d), and IrO_2/Ta_2O_5-Ti (e) electrodes in the non-Faraday region.

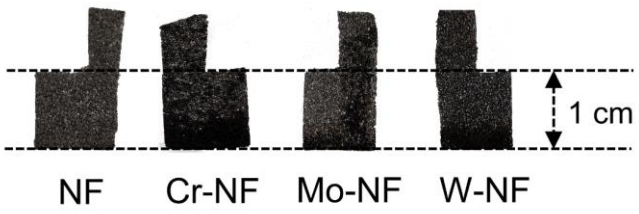

Figure S6. Digital images of NF, Cr-NF, Mo-NF, and W-NF electrodes after the stability test for 5 h at 10 mA cm^{-2}.

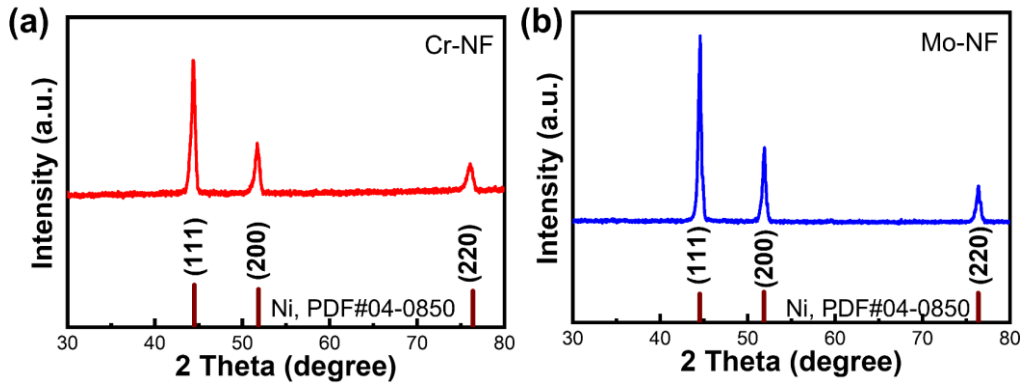

Figure S7. XRD patterns of Cr-NF (a) and Mo-NF (b) electrodes after stability test for 5 h at 10 mA cm^{-2}.

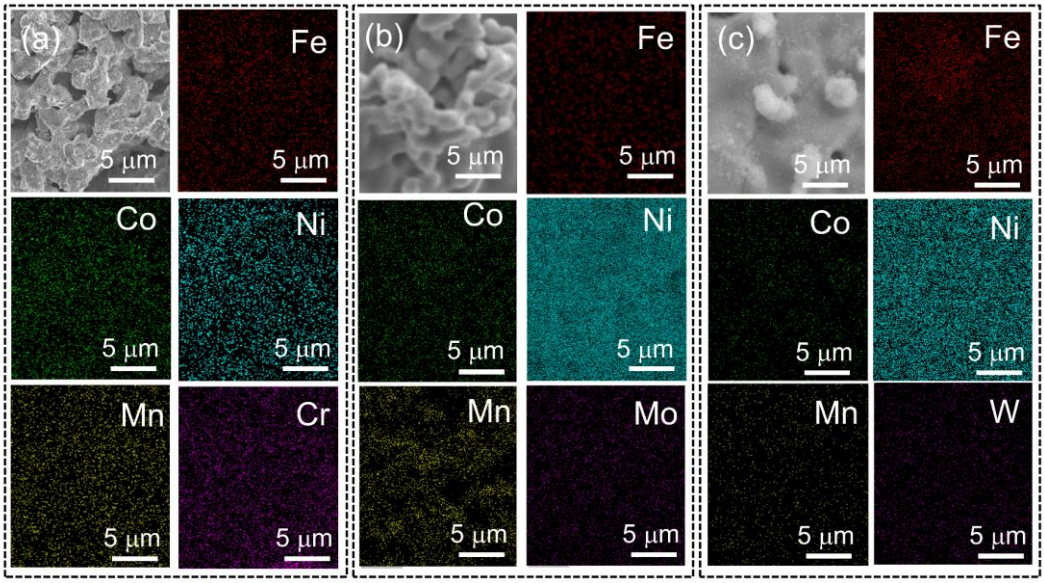

Figure S8. SEM-EDS images after the stability test of Cr-NF for 5 h at 100 mA cm^{-2} (a), Mo-NF for 5 h at 100 mA cm^{-2} (b), and W-NF for 1200 h at 500 mA cm^{-2} (c).

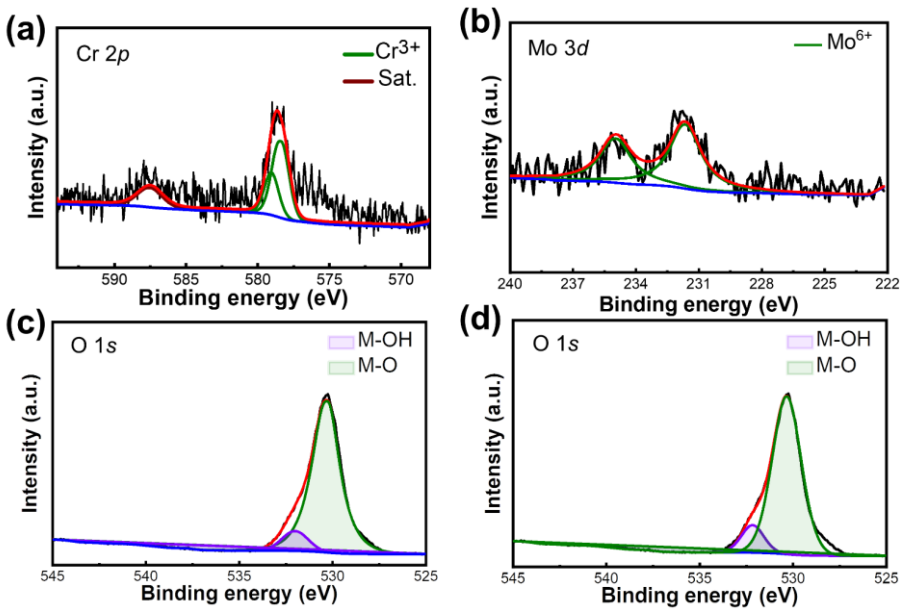

Figure S9. XPS spectra of Cr 2p (a), Mo 3d (b), and O 1s (c, d) of Cr-NF and Mo-NF after the stability test for 5h at 100 mA cm^{-2}.

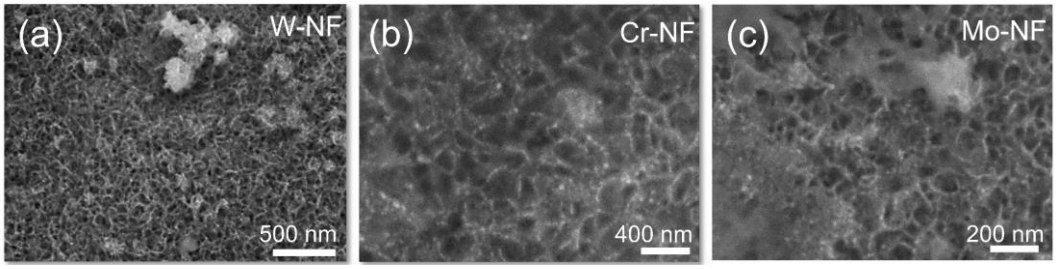

Figure S10. The SEM image of the W-NF (a), Cr-NF (b), and Mo-NF (c) after the stability test for 5h at 100 mA cm^{-2}.

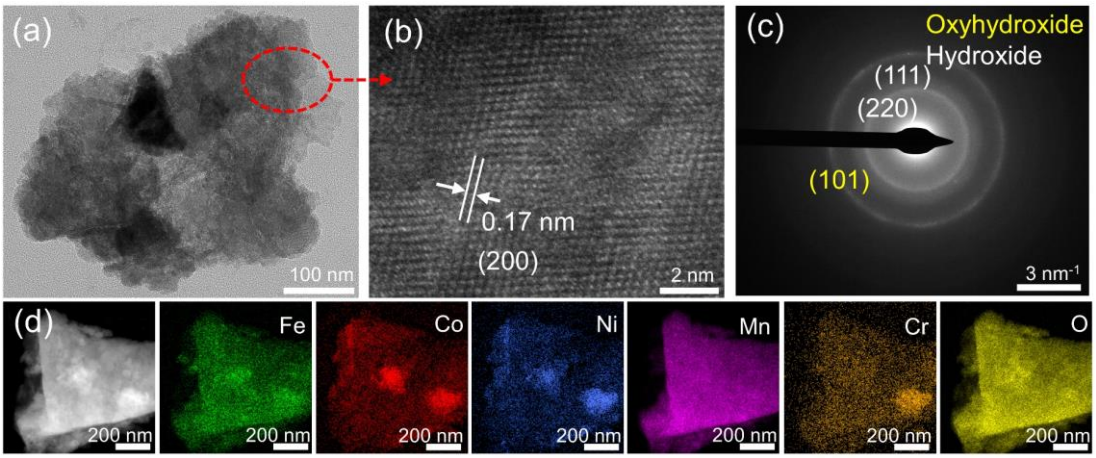

Figure S11. HRTEM image (a), HAADF-STEM image (b, c), and the corresponding EDS mapping (d) of the Cr-NF electrode after durability test for 5 h at 100 mA cm^{-2}.

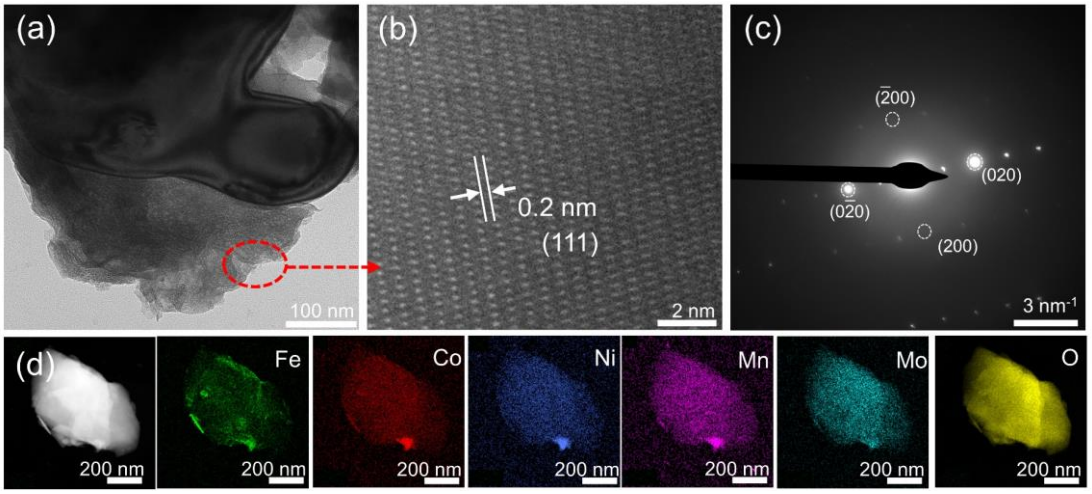

Figure S12. TEM image (a), HAADF-STEM image (b, c), and the corresponding EDS mapping (d) of the Mo-NF electrode after a stability test for 5 h at 100 mA cm^{-2}.

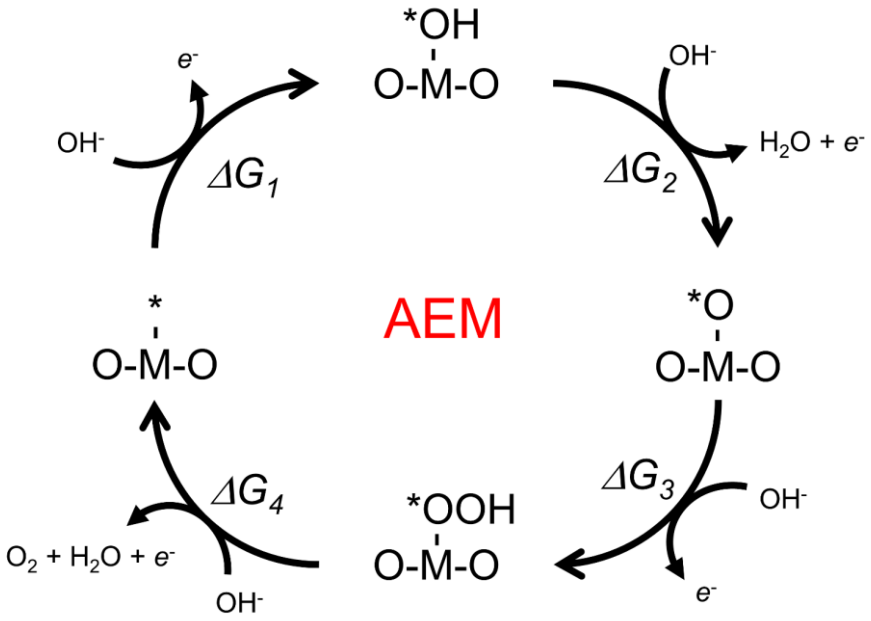

Figure S13. The schematic graphic of the adsorbate evolution mechanism (AEM).

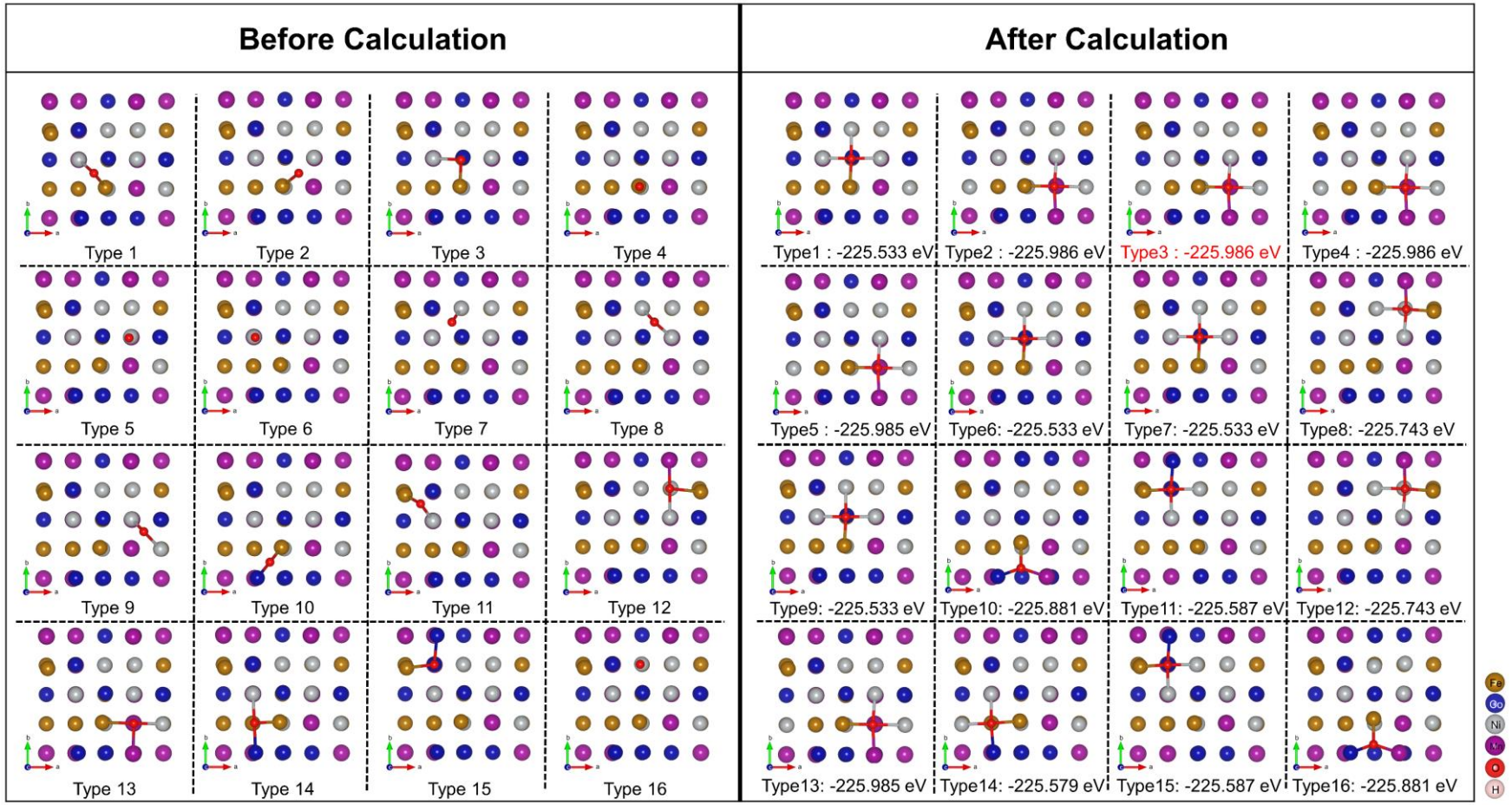

Figure S14. The different types of adsorption sites for *O on FeCoNiMn.

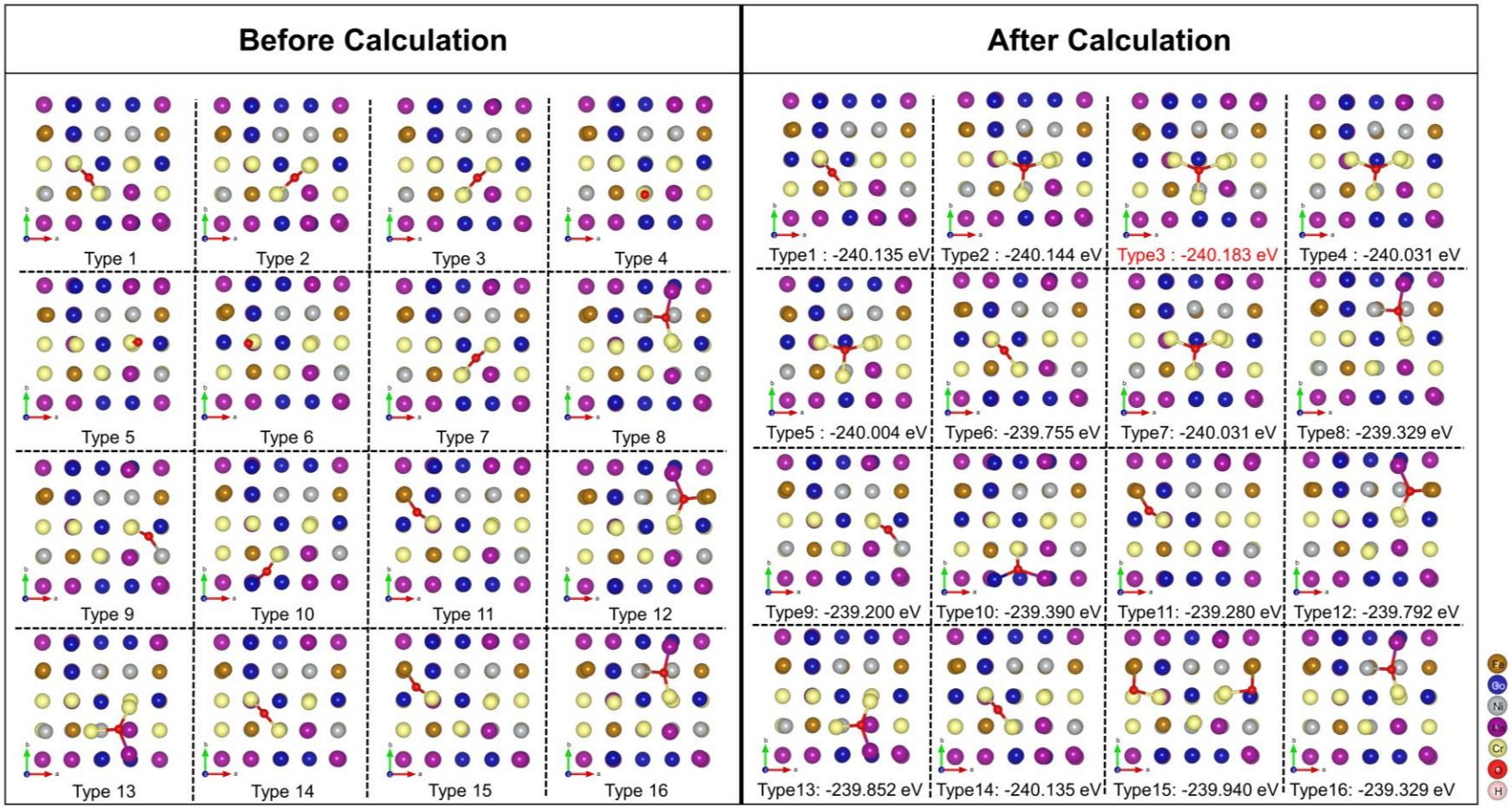

Figure S15. The different types of adsorption sites for *O on FeCoNiMnCr.

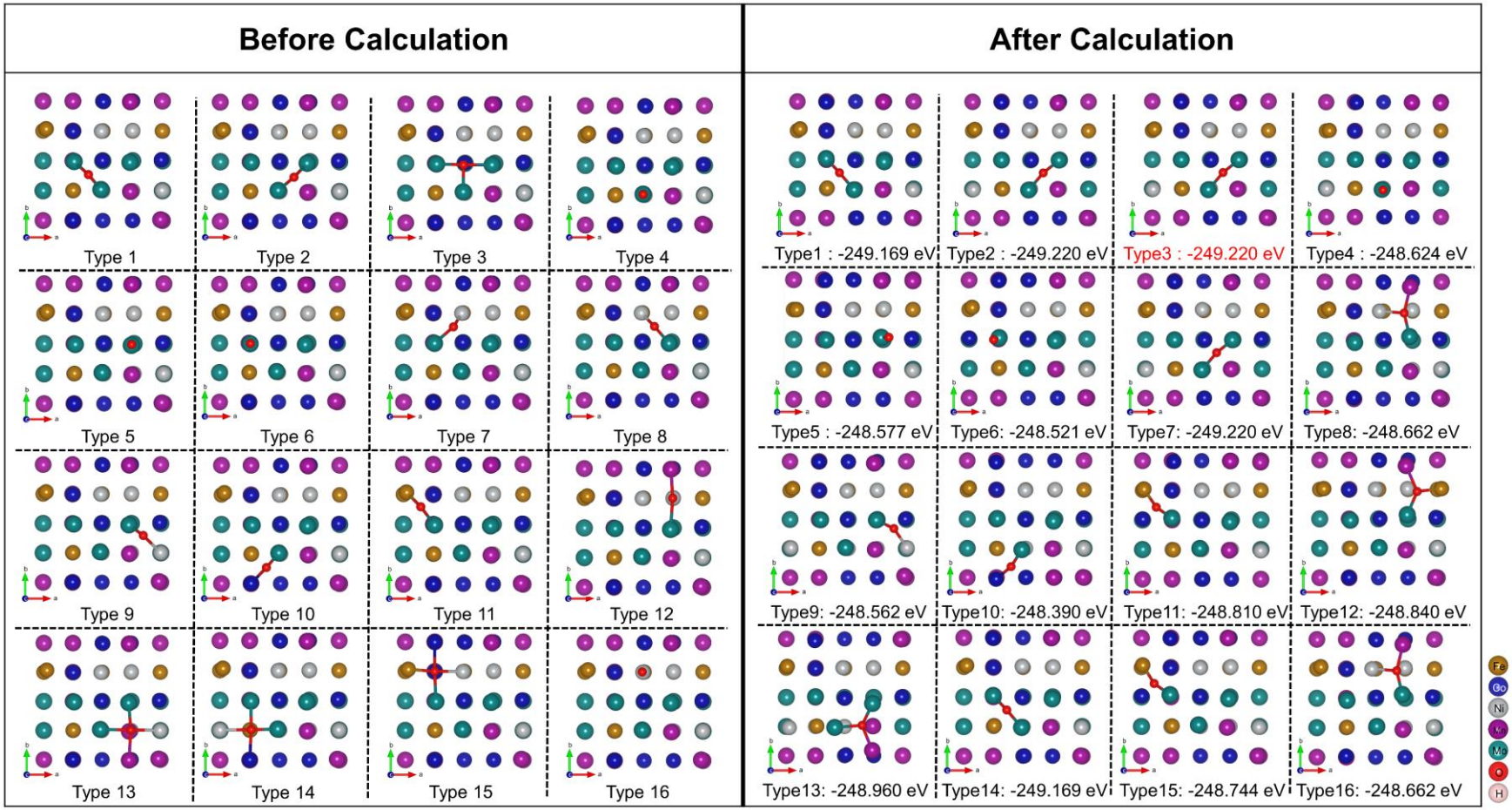

Figure S16. The different types of adsorption sites for *O on FeCoNiMnMo.

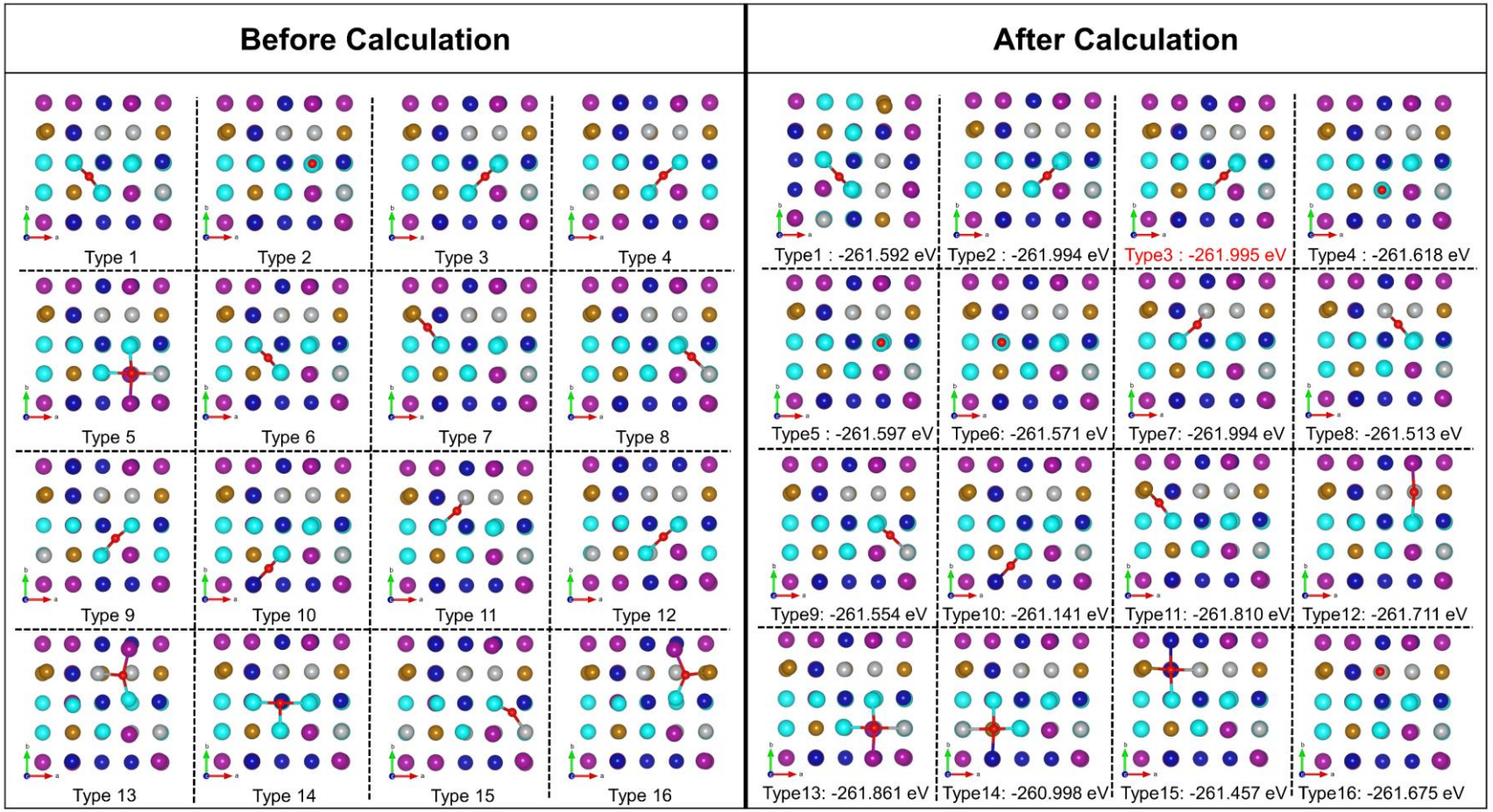

Figure S17. The different types of adsorption sites for *O on FeCoNiMnW.

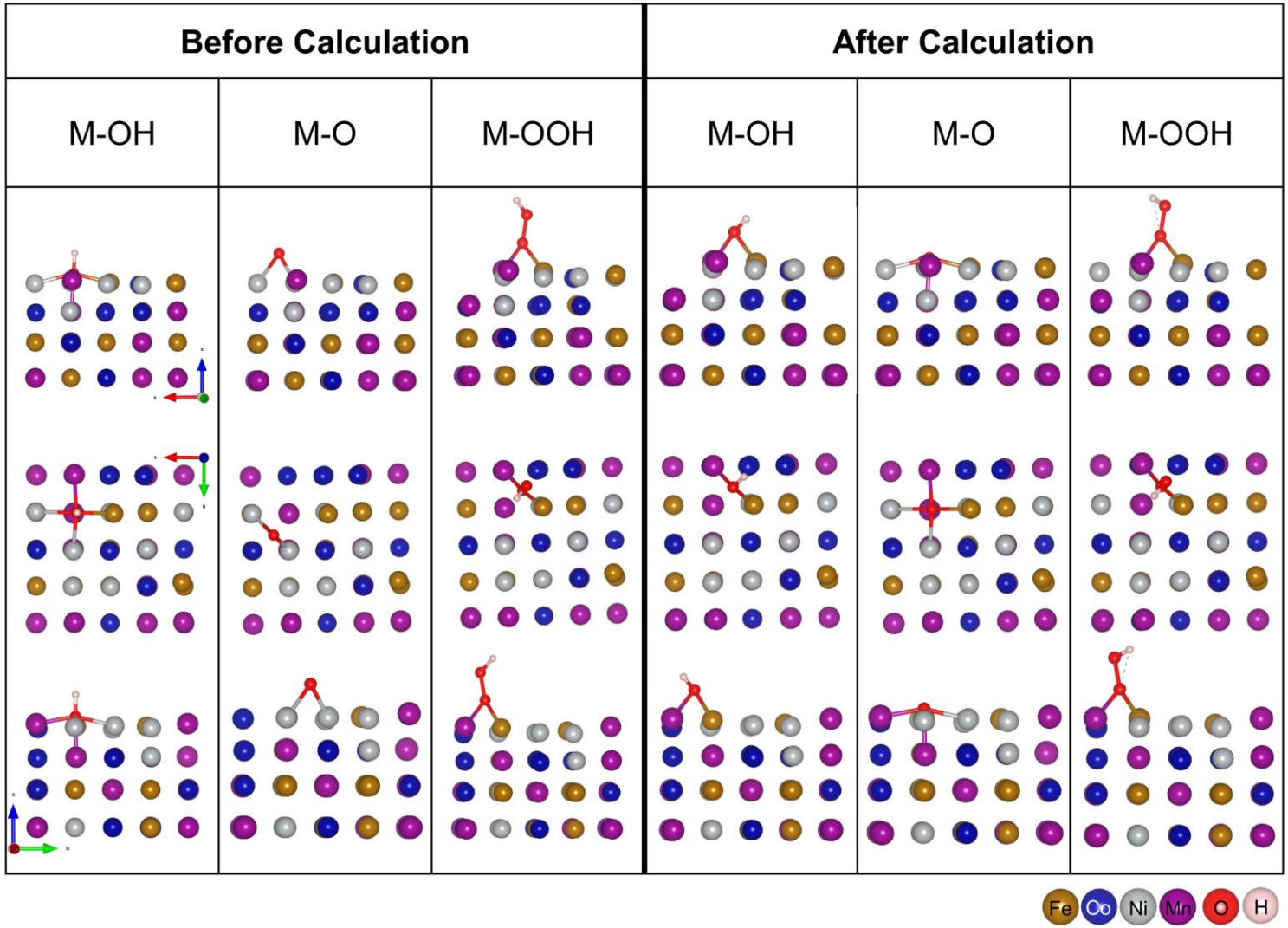

Figure S18. Model changes (three-view drawing) of the adsorption of *OH, *O, and *OOH on FeCoNiMn electrodes before and after the OER process.

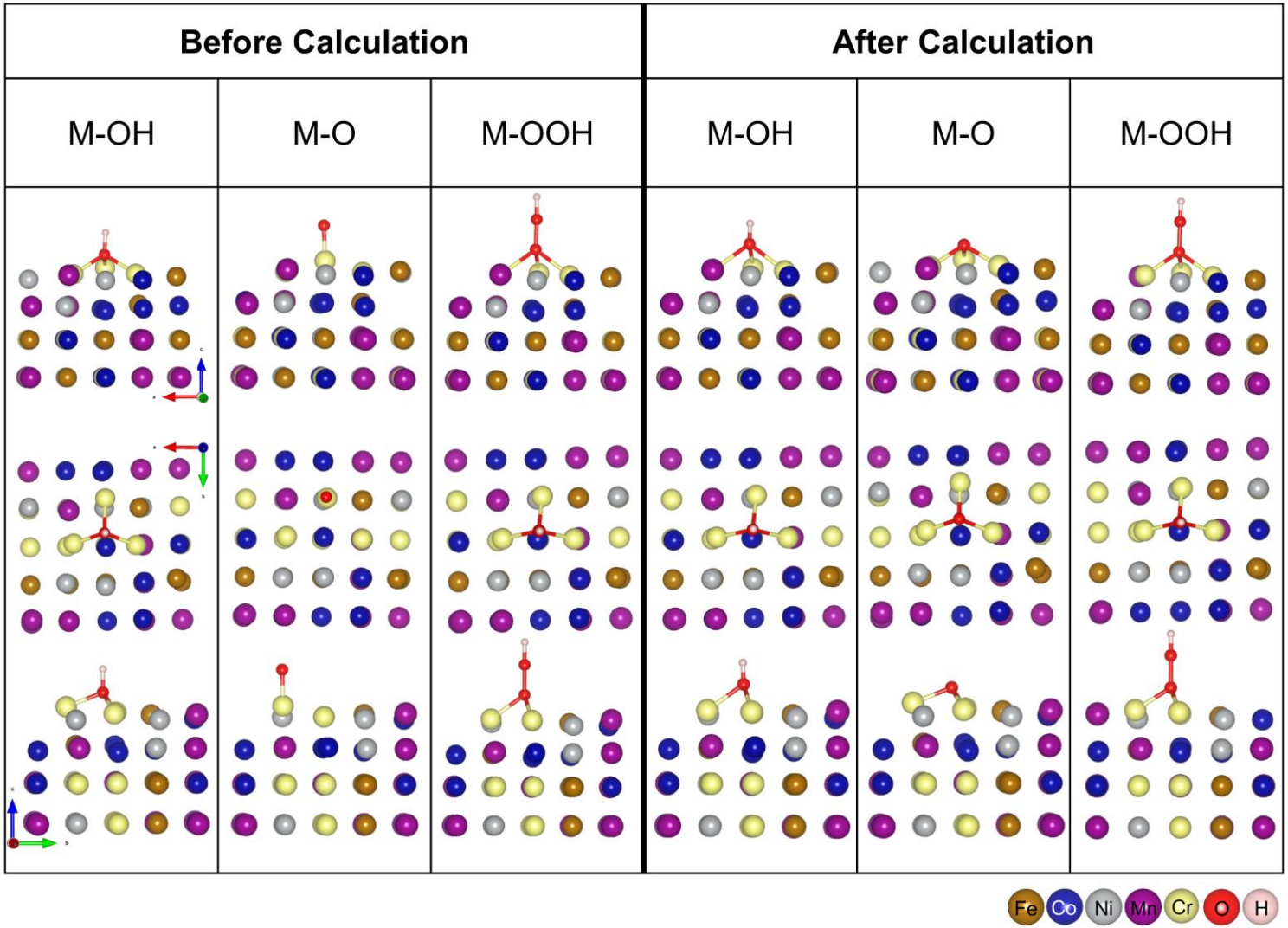

Figure S19. Model changes (three-view drawing) of the adsorption of *OH, *O, and *OOH on FeCoNiMnCr electrodes before and after the OER process.

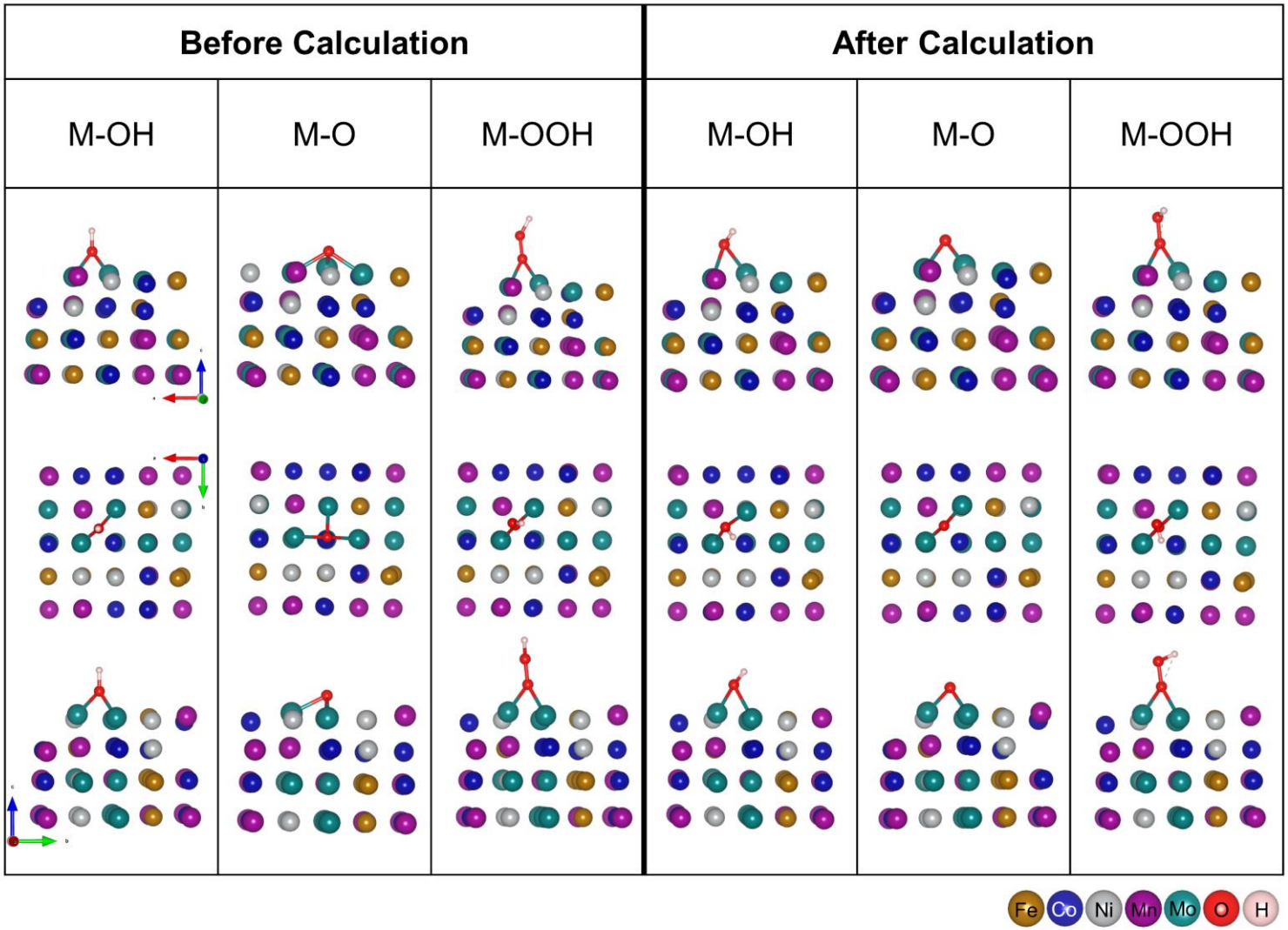

Figure S20. Model changes (three-view drawing) of the adsorption of *OH, *O, and *OOH on FeCoNiMnMo electrodes before and after the OER process.

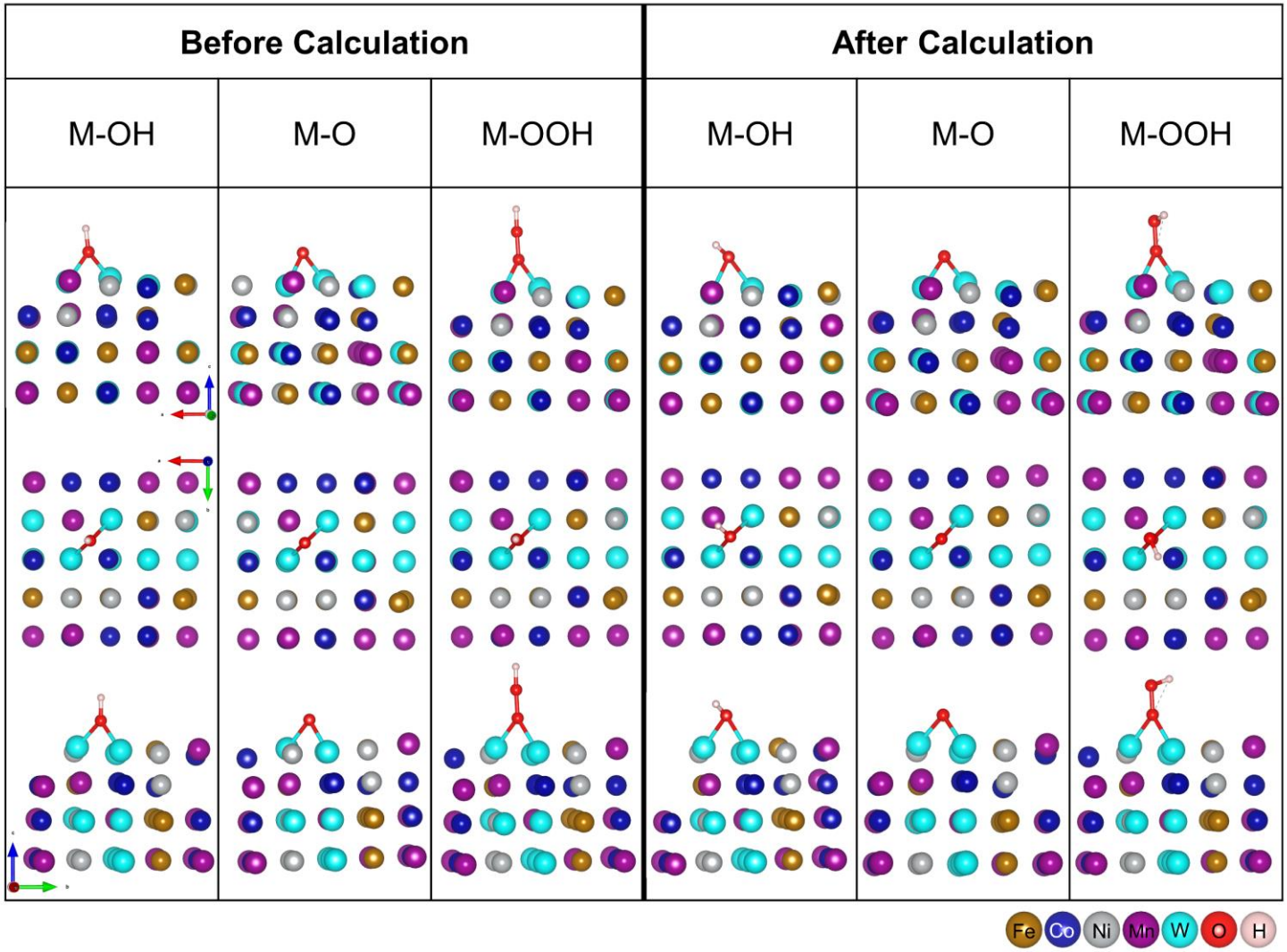

Figure S21. Model changes (three-view drawing) of the adsorption of *OH, *O, and *OOH on FeCoNiMnW electrodes before and after the OER process.

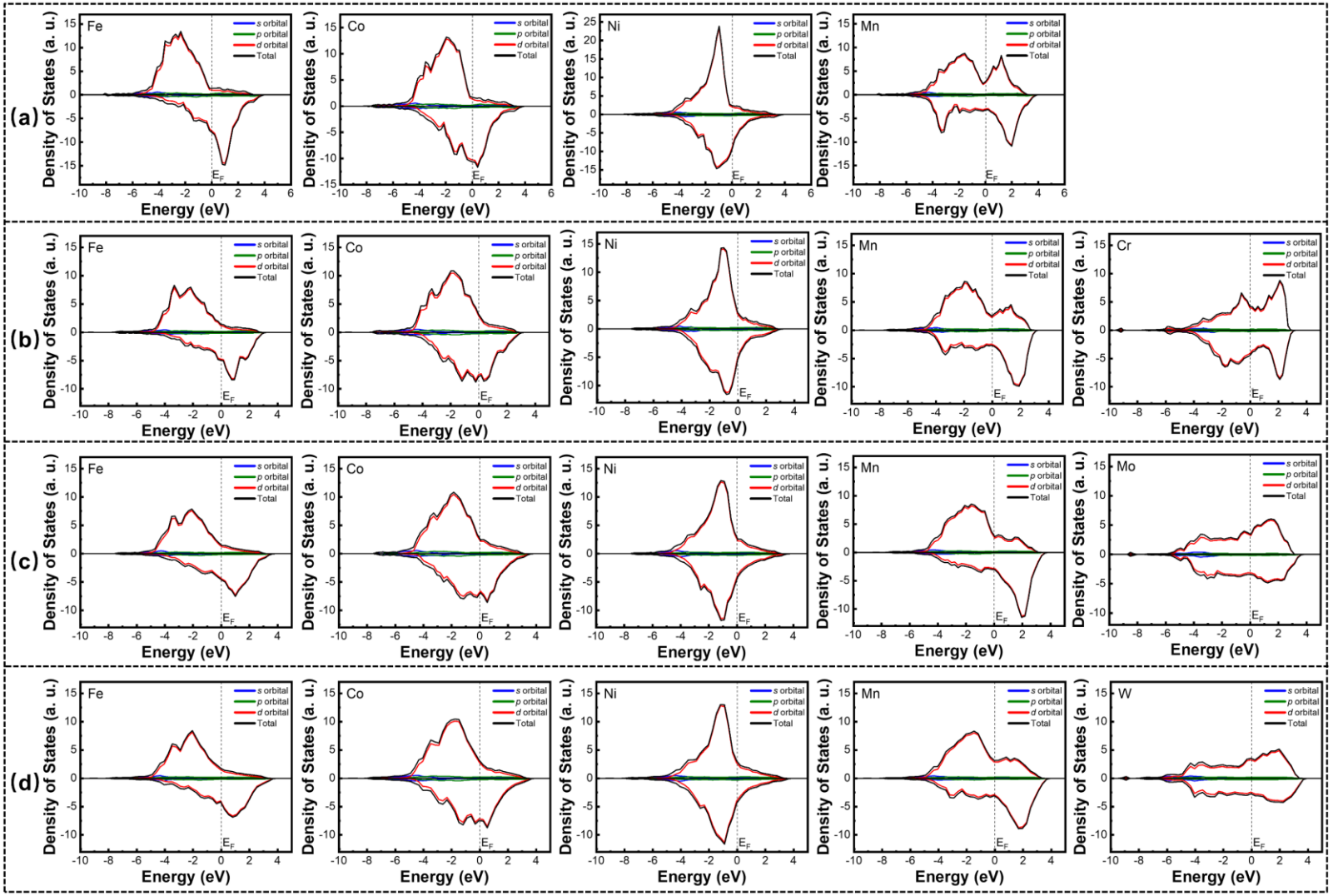

Figure S22. The spin-dependent projected density of states (PDOS) of FeCoNiMn (a), FeCoNiMnCr (b), FeCoNiMnMo (c), and FeCoNiMnW (d) electrodes.

Figure S23. Digital graphs of the scale-up electrode (40 × 500 mm) before preparation.

3. Supporting Tables

Table S1. The weight change of NF, Cr-NF, Mo-NF, and W-NF electrodes.

Electrode	Initial weight (pure NF) / g	Weight after loading oxides / g	Weight after reduction / g
Cr-NF	0.60601	0.62531	0.61964
Mo-NF	0.60830	0.63017	0.62407
W-NF	0.63759	0.65673	0.65185

Table S2. Gibbs free energies (ΔG) and theoretical decomposition voltages (ΔE) of $CaCl_2$ and the oxides used in this work at 900ºC.

Reactions	ΔG / kJ	ΔE / V
$CaCl_2 = Ca + Cl_2(g)$	623.491	3.231
$2CaO=2Ca+O_2(g)$	1023.514	2.652
$Fe_2O_3=2Fe+1.5O_2(g)$	516.287	0.892
$Co_3O_4=3Co+2O_2(g)$	460.145	0.596
$2NiO=2Ni+O_2(g)$	267.152	0.692
$MnO_2=Mn+O2(g)$	308.893	0.800
$CrO_3=Cr+1.5O_2(g)$	311.070	0.537
$MoO_2=Mo+O_2(g)$	376.615	0.976
$WO_2=W+O_2(g)$	337.868	0.875

Table S3. Summary of OER activities of NF, Cr-NF, Mo-NF, and W-NF in 1.0 M KOH.

Electrode	η_{10}	η_{100}	η_{500}	Tafel slope	j_0	R_s
	(mV)	(mV)	(mV)	(mV dec^{-1})	(mA cm^{-2})	(Ω)
NF	380	566	898	103.9	2.01×10^{-3}	0.91
Cr-NF	260	393	747	82.6	5.49×10^{-3}	1.17
Mo-NF	259	341	501	70.3	2.71×10^{-3}	1.05
W-NF	243	292	355	41.5	2.16×10^{-2}	0.74
IrO_2/Ta_2O_5-Ti	305	478	872	122.4	3.22×10^{-3}	0.89

η_{10}, η_{100}, η_{500} mean the overpotential (mV vs. RHE) at 10, 100 and 500 mA cm^{-2}. R_s means the solution resistance.

The exchange current densities (j_0) are obtained from Tafel plots.

Table S4. The comparison of OER performances in 1.0 M KOH between this work and other self-supported electrodes.

Electrode	η_{500} (mV)	Tafel slop (mV dec^{-1})	Stability time (h)	Reference
W-NF	355	41.5	$1200_{@500}$	This work
AerMet 100 steel	855	44	$140_{@570}$	[8]
Se-SS	285	36	$95_{@500}$	[9]
$Fe_{50}Ni_{50}$	620*	NA	$25_{@500}$	[10]
CoP-400-IO	670*	46	$90_{@500}$	[11]
FeOx/CFC-8	620*	93	$15_{@50}$	[12]
Co_3O_4-Mo_2N NFs	NA	87.8	$20_{@10}$	[13]
NiFe-NFF	310	38.9	$5_{@20}$	[14]
IISERP-COF3	615*	79	$20_{@50}$	[15]
IF-$NiCl_2$	291	18.3	$100_{@500}$	[16]
VO_x/Ni_3S_2@NF	780*	NA	$10_{@60}$	[17]
Ni_3FeN@C/ NF	330	45	$100_{@500}$	[18]
NiFe-MOF@ Ni_3N/NF	295	54	$50_{@200}$	[19]
O-NFS-ECT	300	39	$18_{@165}$	[20]
Ni_2P@$FePO_xH_y$	319	43	$12_{@100}$	[21]
SSFS	345	42	$40_{@50}$	[22]
NiCo-LDH	NA	113	$1.1_{@730}$	[23]
Ni-Fe-OH@Ni_3S_2/NF	426	93	$50_{@500}$	[24]
Co@NiFe-LDH	NA	44	$50_{@10}$	[25]

η_{500} : the overpotential (mV vs. RHE) at 500 mA cm^{-2}.

*: Inferred from the LSV curves.

NA: not available

The subscript of stability time indicates the current density during the stability test, e.g., $1200_{@500}$ means the test duration is 1200 h at 500 mA cm^{-2}.

Table S5. Comparison of catalytic performance parameters of NF, Cr-NF, Mo-NF, W-NF, and IrO_2/Ta_2O_5-Ti electrodes.

Electrodes	C_{dl} / mF cm^{-2}	ECSA / cm^2	TOF / s^{-1}	Potential changed value / mV
NF	1.54	38.5	0.039	-
Cr-NF	7.54	188.5	0.113	20.6
Mo-NF	9.63	240.8	0.169	16.1
W-NF	28.6	715.0	0.227	13.8
IrO_2/Ta_2O_5-Ti	26.3	657.5	0.051	72.4

Table S6. The ratio of M-OH and M-O bonds of Cr-NF, Mo-NF, and W-NF after the stability test.

Electrode	M-OH (%)	M-O (%)
Cr-NF	9.8	90.2
Mo-NF	8.4	91.6
W-NF	5.4	94.6

4. Supporting References

(1) Chen, S.; Duan, J.; Bian, P.; Tang, Y.; Zheng, R.; Qiao, S.-Z. Three-Dimensional Smart Catalyst Electrode for Oxygen Evolution Reaction. *Adv. Energy. Mater.* **2015**, *5* (18), 1500936, DOI: 10.1002/aenm.201500936.

(2) Tahir, M.; Pan, L.; Idrees, F.; Zhang, X.; Wang, L.; Zou, J.-J.; Wang, Z. L. Electrocatalytic Oxygen Evolution Reaction for Energy Conversion and Storage: A Comprehensive Review. *Nano. Energy.* **2017**, *37*, 136–157, DOI: 10.1016/j.nanoen.2017.05.022.

(3) Kim, Y. T.; Lopes, P. P.; Park, S. A.; Lee, A. Y.; Lim, J.; Lee, H.; Back, S.; Jung, Y.; Danilovic, N.; Stamenkovic, V.; Erlebacher, J.; Snyder, J.; Markovic, N. M. Balancing Activity, Stability and Conductivity of Nanoporous Core-Shell Iridium/Iridium Oxide Oxygen Evolution Catalysts. *Nat. Commun.* **2017**, *8* (1), 1449, DOI: 10.1038/s41467-017-01734-7.

(4) Zhou, T.; Cao, Z.; Zhang, P.; Ma, H.; Gao, Z.; Wang, H.; Lu, Y.; He, J.; Zhao, Y. Transition Metal Ions Regulated Oxygen Evolution Reaction Performance of Ni-Based Hydroxides Hierarchical Nanoarrays. *Sci. Rep.* **2017**, *7*, 46154, DOI: 10.1038/srep46154.

(5) Zheng, J. Pt-Free NiCo Electrocatalysts for Oxygen Evolution by Seawater Splitting. *Electrochim. Acta.* **2017**, *247*, 381–391, DOI: 10.1016/j.electacta.2017.07.024.

(6) Pan, Y.; Xu, X.; Zhong, Y.; Ge, L.; Chen, Y.; Veder, J. P. M.; Guan, D.; O'Hayre, R.; Li, M.; Wang, G.; Wang, H.; Zhou, W.; Shao, Z. Direct Evidence of Boosted Oxygen Evolution over Perovskite by Enhanced Lattice Oxygen Participation. *Nat. Commun.* **2020**, *11* (1), 2002, DOI: 10.1038/s41467-020-15873-x.

(7) Zhang, L.; Cai, W.; Bao, N.; Yang, H. Implanting an Electron Donor to Enlarge the d–p Hybridization of High-Entropy (Oxy)Hydroxide: A Novel Design to Boost Oxygen Evolution. *Adv. Mater.* **2022**, *34* (26), 2110511, DOI: 10.1002/adma.202110511.

(8) Zhou, P.; Niu, P.; Liu, J.; Zhang, N.; Bai, H.; Chen, M.; Feng, J.; Liu, D.; Wang, L.; Chen, S.; Kwok, C. T.; Tang, Y.; Li, R.; Wang, S.; Pan, H. Anodized Steel: The Most Promising Bifunctional Electrocatalyst for Alkaline Water Electrolysis in Industry. *Adv. Funct. Mater.* **2022**, *32* (26), 2202068, DOI: 10.1002/adfm.202202068.

(9) Xiao, Y.; Hu, T.; Zhao, X.; Hu, F. X.; Yang, H. Bin; Li, C. M. Thermo-Selenizing to Rationally Tune Surface Composition and Evolve Structure of Stainless Steel to Electrocatalytically Boost Oxygen Evolution Reaction. *Nano Energy.* **2020**, *75*, 104949, DOI: 10.1016/j.nanoen.2020.104949.

(10) Guo, F.; Wu, Y.; Chen, H.; Liu, Y.; Yang, L.; Ai, X.; Zou, X. High-Performance Oxygen Evolution Electrocatalysis by Boronized Metal Sheets with Self-Functionalized Surfaces. *Energy. Environ. Sci.* **2019**, *12* (2), 684–692, DOI: 10.1039/c8ee03405b.

(11) Yu, X.; Wang, M.; Gong, X.; Guo, Z.; Wang, Z.; Jiao, S. Self-Supporting Porous CoP-Based Films with Phase-Separation Structure for Ultrastable Overall Water Electrolysis at Large Current Density. *Adv. Energy. Mater.* **2018**, *8* (34), 1802445, DOI: 10.1002/aenm.201802445.

(12) Yan, F.; Zhu, C.; Wang, S.; Zhao, Y.; Zhang, X.; Li, C.; Chen, Y. Electrochemically Activated-Iron Oxide Nanosheet Arrays on Carbon Fiber Cloth as a Three-Dimensional Self-Supported Electrode for Efficient Water Oxidation. *J. Mater. Chem. A. Mater.* **2016**, *4* (16), 6048–6055, DOI: 10.1039/c6ta00456c.

(13) Wang, T.; Wang, P.; Zang, W.; Li, X.; Chen, D.; Kou, Z.; Mu, S.; Wang, J. Nanoframes of Co_3O_4–Mo_2N Heterointerfaces Enable High-Performance Bifunctionality toward Both Electrocatalytic HER and OER. *Adv. Funct. Mater.* **2022**, *32* (7), 2107382, DOI: 10.1002/adfm.202107382.

(14) Cao, C.; Ma, D. D.; Xu, Q.; Wu, X. T.; Zhu, Q. L. Semisacrificial Template Growth of Self-Supporting MOF Nanocomposite Electrode for Efficient Electrocatalytic Water Oxidation. *Adv. Funct. Mater.* **2019**, *29* (6), 1807418, DOI: 10.1002/adfm.201807418.

(15) Nandi, S.; Singh, S. K.; Mullangi, D.; Illathvalappil, R.; George, L.; Vinod, C. P.; Kurungot, S.; Vaidhyanathan, R. Low Band Gap Benzimidazole COF Supported Ni_3N as Highly Active OER Catalyst. *Adv. Energy. Mater.* **2016**, *6* (24), 1601189, DOI: 10.1002/aenm.201601189.

(16) Liu, X.; Guo, X.; Gong, M.; Zhao, T.; Zhang, J.; Zhu, Y.; Wang, D. Regulated Iron Corrosion towards Fabricating Large-Area Self-Supporting Electrodes for an Efficient Oxygen Evolution Reaction. *J. Mater. Chem. A. Mater.* **2021**, *9* (40), 23188–23198, DOI:

10.1039/d1ta06370g.

(17) Niu, Y.; Li, W.; Wu, X.; Feng, B.; Yu, Y.; Hu, W.; Li, C. M. Amorphous Nickel Sulfide Nanosheets with Embedded Vanadium Oxide Nanocrystals on Nickel Foam for Efficient Electrochemical Water Oxidation. *J. Mater. Chem. A. Mater.* **2019**, *7* (17), 10534–10542, DOI: 10.1039/c8ta12483c.

(18) Wang, B.; Lu, M.; Chen, D.; Zhang, Q.; Wang, W.; Kang, Y.; Fang, Z.; Pang, G.; Feng, S. Ni_xFe_yN@C Microsheet Arrays on Ni Foam as an Efficient and Durable Electrocatalyst for Electrolytic Splitting of Alkaline Seawater. *J. Mater. Chem. A. Mater.* **2021**, *9* (23), 13562–13569, DOI: 10.1039/d1ta01292d.

(19) Wang, B.; Chen, D.; Jiao, S.; Zhang, Q.; Wang, W.; Lu, M.; Fang, Z.; Pang, G.; Feng, S. Coupling NiFe-MOF Nanosheets with Ni_3N Microsheet Arrays for Efficient Electrocatalytic Water Oxidation. *New J. Chem.* **2021**, *45* (42), 19646–19650, DOI: 10.1039/d1nj03730g.

(20) Zhang, J.; Hu, Y.; Liu, D.; Yu, Y.; Zhang, B. Enhancing Oxygen Evolution Reaction at High Current Densities on Amorphous-like Ni-Fe-S Ultrathin Nanosheets via Oxygen Incorporation and Electrochemical Tuning. *Adv. Sci.* **2017**, *4* (3), 1600343, DOI: 10.1002/advs.201600343.

(21) Meena, A.; Thangavel, P.; Jeong, D. S.; Singh, A. N.; Jana, A.; Im, H.; Nguyen, D. A.; Kim, K. S. Crystalline-Amorphous Interface of Mesoporous Ni_2P@$FePO_xH_y$ for Oxygen Evolution at High Current Density in Alkaline-Anion-Exchange-Membrane Water-Electrolyzer. *Appl. Catal. B.* **2022**, *306*, 121127, DOI: 10.1016/j.apcatb.2022.121127.

(22) Liu, X.; You, B.; Sun, Y. Facile Surface Modification of Ubiquitous Stainless Steel Led to Competent Electrocatalysts for Overall Water Splitting. *ACS Sustain. Chem. Eng.* **2017**, *5* (6), 4778–4784, DOI: 10.1021/acssuschemeng.7b00182.

(23) Jiang, J.; Zhang, A.; Li, L.; Ai, L. Nickel-Cobalt Layered Double Hydroxide Nanosheets as High-Performance Electrocatalyst for Oxygen Evolution Reaction. *J. Power. Sources.* **2015**, *278*, 445–451, DOI: 10.1016/j.jpowsour.2014.12.085.

(24) Zou, X.; Liu, Y.; Li, G. D.; Wu, Y.; Liu, D. P.; Li, W.; Li, H. W.; Wang, D.; Zhang, Y.; Zou, X. Ultrafast Formation of Amorphous Bimetallic Hydroxide Films on 3D Conductive Sulfide

Nanoarrays for Large-Current-Density Oxygen Evolution Electrocatalysis. *Adv. Mater.* **2017**, *29* (22), 1700404, DOI: 10.1002/adma.201700404.

(25) Liu, S.; Wan, R.; Lin, Z.; Liu, Z.; Liu, Y.; Tian, Y.; Qin, D.-D.; Tang, Z. Probing the Co Role in Promoting the OER and Zn–Air Battery Performance of NiFe-LDH: A Combined Experimental and Theoretical Study. *J. Mater. Chem. A. Mater.* **2022**, *10* (10), 5244–5254, DOI: 10.1039/d1ta11055a.